HAL
open science

QUIJOTE scientific results - V. The microwave intensity and polarization spectra of the Galactic regions W49, W51 and IC443

D. Tramonte, R. T. Génova-Santos, J. A. Rubiño-Martín, P. Vielva, F. Poidevin, C. H. López-Caraballo, M. W. Peel, M. Ashdown, E. Artal, R. B. Barreiro, et al.

To cite this version:

D. Tramonte, R. T. Génova-Santos, J. A. Rubiño-Martín, P. Vielva, F. Poidevin, et al.. QUIJOTE scientific results - V. The microwave intensity and polarization spectra of the Galactic regions W49, W51 and IC443. Monthly Notices of the Royal Astronomical Society, 2023, 519, pp.3432-3459. 10.1093/mnras/stac3502 . insu-03947306

HAL Id: insu-03947306

https://insu.hal.science/insu-03947306v1

Submitted on 18 Jul 2023

HAL is a multi-disciplinary open access archive for the deposit and dissemination of scientific research documents, whether they are published or not. The documents may come from teaching and research institutions in France or abroad, or from public or private research centers.

L'archive ouverte pluridisciplinaire **HAL**, est destinée au dépôt et à la diffusion de documents scientifiques de niveau recherche, publiés ou non, émanant des établissements d'enseignement et de recherche français ou étrangers, des laboratoires publics ou privés.

Monthly Notices of the ROYAL ASTRONOMICAL SOCIETY

MNRAS **519,** 3432–3459 (2023) https://doi.org/10.1093/mnras/stac3502

QUIJOTE scientific results – V. The microwave intensity and polarization spectra of the Galactic regions W49, W51 and IC443

D. Tramonte,[1,2,3,4★] R. T. Génova-Santos,[3,4] J. A. Rubiño-Martín,[3,4] P. Vielva,[5] F. Poidevin,[3,4] C. H. López-Caraballo,[3,4] M. W. Peel,[3,4] M. Ashdown,[6,7] E. Artal,[8] R. B. Barreiro,[5] F. J. Casas,[5] E. de la Hoz,[5,9] M. Fernández-Torreiro,[3,4] F. Guidi,[3,4,10] D. Herranz,[5] R. J. Hoyland,[3,4] A. N. Lasenby,[6,7] E. Martinez-Gonzalez,[5] L. Piccirillo,[11] R. Rebolo,[3,4,12] B. Ruiz-Granados,[3,4,13] F. Vansyngel[3,4] and R. A. Watson[11]

[1]*Purple Mountain Observatory, CAS, No. 10 Yuanhua Road, Qixia District, Nanjing 210034, China*
[2]*NAOC-UKZN Computational Astrophysics Center (NUCAC), University of Kwazulu-Natal, Durban 4000, South Africa*
[3]*Instituto de Astrofísica de Canarias, E-38200 La Laguna, Tenerife, Spain*
[4]*Departamento de Astrofísica, Universidad de La Laguna, E-38206 La Laguna, Tenerife, Spain*
[5]*Instituto de Física de Cantabria (IFCA), CSIC-Univ. de Cantabria, Avda. los Castros, s/n, E-39005 Santander, Spain*
[6]*Astrophysics Group, Cavendish Laboratory, University of Cambridge, J J Thomson Avenue, Cambridge CB3 0HE, UK*
[7]*Kavli Institute for Cosmology, University of Cambridge, Madingley Road, Cambridge CB3 0HA, UK*
[8]*Departamento de Ingeniería de COMunicaciones (DICOM), Universidad de Cantabria, Plaza de la Ciencia s/n, E-39005 Santander, Spain*
[9]*Dpto. de Física Moderna, Universidad de Cantabria, Avda. los Castros s/n, E-39005 Santander, Spain*
[10]*Institut d'Astrophysique de Paris, UMR 7095, CNRS & Sorbonne Université, 98 bis boulevard Arago, F-75014 Paris, France*
[11]*Jodrell Bank Centre for Astrophysics, Alan Turing Building, Department of Physics and Astronomy, School of Nature Sciences, University of Manchester, Oxford Road, Manchester M13 9PL, UK*
[12]*Consejo Superior de Investigaciones Cientificas, E-28006 Madrid, Spain*
[13]*Departamento de Física. Facultad de Ciencias. Universidad de Córdoba. Campus de Rabanales, Edif. C2. Planta Baja. E-14071 Córdoba, Spain*

Accepted 2022 November 25. Received 2022 November 20; in original form 2022 July 28

ABSTRACT

We present new intensity and polarization maps obtained with the QUIJOTE experiment towards the Galactic regions W49, W51 and IC443, covering the frequency range from 10 to 20 GHz at ~ 1 deg angular resolution, with a sensitivity in the range 35–79 μK beam^{-1} for total intensity and 13–23 μK beam^{-1} for polarization. For each region, we combine QUIJOTE maps with ancillary data at frequencies ranging from 0.4 to 3000 GHz, reconstruct the spectral energy distribution and model it with a combination of known foregrounds. We detect anomalous microwave emission (AME) in total intensity towards W49 at 4.7σ and W51 at 4.0σ with peak frequencies $\nu_{\rm AME} = (20.0 \pm 1.4)$ GHz and $\nu_{\rm AME} = (17.7 \pm 3.6)$ GHz, respectively; this is the first detection of AME towards W51. The contamination from ultracompact H II regions to the residual AME flux density is estimated at 10 per cent in W49 and 5 per cent in W51, and does not rule out the AME detection. The polarized SEDs reveal a synchrotron contribution with spectral indices $\alpha_{\rm s} = -0.67 \pm 0.10$ in W49 and $\alpha_{\rm s} = -0.51 \pm 0.07$ in W51, ascribed to the diffuse Galactic emission and to the local supernova remnant, respectively. Towards IC443 in total intensity we measure a broken power-law synchrotron spectrum with cut-off frequency $\nu_{0,\rm s} = (114 \pm 73)$ GHz, in agreement with previous studies; our analysis, however, rules out any AME contribution which had been previously claimed towards IC443. No evidence of polarized AME emission is detected in this study.

Key words: radiation mechanisms: general – ISM: individual objects: W49, W51, IC443 – radio continuum: ISM.

1 INTRODUCTION

During the past two decades, the study of the cosmic microwave background (CMB) anisotropies allowed us to estimate cosmological parameters to the per cent precision level, and led to the establishment of the Lambda-Cold Dark Matter (ΛCDM) cosmology as the most widely accepted paradigm describing our Universe (Hinshaw et al. 2013; Planck Collaboration VI 2020b). The most recent endeavors are focusing on the characterization of CMB polarization, in particular on the search for the inflationary B-mode anisotropies (Kamionkowski, Kosowsky & Stebbins 1997; Zaldarriaga & Seljak 1997). However, to date only upper limits on the level of primordial B-modes anisotropies are available (Planck Collaboration VI 2020c; Ade et al. 2021; BICEP/Keck Collaboration 2021), as this signal is subdominant compared to other polarized Galactic and extra-Galactic emissions. An accurate modelling of these foregrounds becomes then of paramount importance, not only

★ E-mail: tramonte@pmo.ac.cn

© 2023 The Author(s)
Published by Oxford University Press on behalf of Royal Astronomical Society

Downloaded from https://academic.oup.com/mnras/article/519/3/3432/6984761 by guest on 18 July 2023

to produce clean CMB maps for their cosmological exploitation, but also to better characterize the physical properties of the interstellar medium (ISM).

In total intensity, the main foregrounds affecting any CMB observations are synchrotron radiation generated by cosmic ray electrons spiralling in the Galactic magnetic field, free–free emission from electron thermal *bremsstrahlung*, thermal radiation from interstellar dust, and the so-called anomalous microwave emission (AME; Planck Collaboration XIII 2016b); to this list of continuum emissions we can also add the contamination from molecular lines (mostly CO). While the mechanisms responsible for the first three continuum foregrounds are physically well understood, the nature of AME is still under debate (for a detailed review we redirect to Dickinson et al. 2018). This emission, first discovered in the mid-90s (Leitch et al. 1997), appears at frequencies ∼10–60 GHz as a dust-correlated signal that cannot be explained in terms of the other foreground components. The most accredited model explaining its origin is the dipole radiation from small, fast spinning dust grains in the ISM (Draine & Lazarian 1998; Ali-Haïmoud, Hirata & Dickinson 2009; Hoang, Draine & Lazarian 2010; Ysard & Verstraete 2010; Silsbee, Ali-Haïmoud & Hirata 2011; Ali-Haïmoud 2013); this scenario is referred to as spinning dust emission (SDE). A different model known as magnetic dust emission (MDE) has also been proposed, according to which the thermal emission from magnetized ISM dust grains is the mechanism responsible for AME (Draine & Lazarian 1999; Draine & Hensley 2013). More recently, models based on thermal emission from amorphous dust grains proved effective in yielding the excess AME signal at microwave frequencies (Nashimoto et al. 2020). Many observational efforts have tackled the detection of AME in the attempt of better characterizing its nature (de Oliveira-Costa et al. 1998, 1999; Finkbeiner et al. 2002; Watson et al. 2005; Casassus et al. 2006; Davies et al. 2006; AMI Consortium 2009; Dickinson et al. 2009; Murphy et al. 2010; Tibbs et al. 2010; Génova-Santos et al. 2011; Planck Collaboration VIII 2011; Vidal et al. 2011; Planck Collaboration XVI 2014a; Battistelli et al. 2015; Vidal et al. 2020). However, up-to-date the results are not clear; a promising way of distinguishing between different AME models is the observation of its polarization.

Out of the aforementioned foregrounds, the free–free emission is known to be practically unpolarized[1] (Rybicki & Lightman 1979; Trujillo-Bueno, Moreno-Insertis & Sánchez 2002), whereas synchrotron and thermal dust emissions yield, respectively, polarization fractions Π up to 40 per cent and 20 per cent in some regions of the sky (Kogut et al. 2007; Vidal et al. 2015; Planck Collaboration XIII 2016b; Planck Collaboration VI 2020e, a). On the contrary, the polarization properties of AME are still under debate. Theoretically, predictions have been made for the spinning dust model; although the dipole emission from an individual dust grain is expected to be linearly polarized, the presence of a detectable polarization fraction in the observed SDE strongly depends on the spatial alignment of ISM grains. Studies of the conditions for grain alignment have been addressed in the literature (Lazarian & Draine 2000; Hoang, Lazarian & Martin 2013) and generally place upper limits for the SDE polarization fraction at the per cent level. The work by Draine & Hensley (2016), however, suggests that at $\nu \gtrsim 10$ GHz quantum effects prevent the dissipation of the grain rotational energy, thereby erasing the alignment and resulting in negligible polarization levels ($\Pi \ll 1$ per cent). The theoretical study of MDE polarization has also been tackled: Draine & Lazarian (1999) and Draine & Hensley (2013) found that in the case of free-flying magnetized grains the resulting polarization fraction can be as high as 30 per cent; a more recent study described in Hoang & Lazarian (2016), however, set the upper limits for the polarized emission fraction from free-flying iron nanoparticles at ∼ 5 per cent. Similar constraints were obtained in the case of magnetic inclusions within larger, non-magnetic grains (Draine & Hensley 2013). The MDE is then expected to provide higher polarization fractions compared to the SDE scenario. The amorphous dust models, finally, found that the AME polarization is suppressed by the contribution from amorphous carbon dust, accounting for nearly half of the ISM grains (Nashimoto et al. 2020).

Observationally, there are no clear detections of AME in polarization to date yet. Polarized AME has been searched for with dedicated observations towards a number of different environments, such as supernova remnants (SNRs), planetary nebulae, or molecular clouds (Rubiño-Martín et al. 2012a). Battistelli et al. (2006) reported a tentative detection towards the Perseus molecular complex using the COSMOlogical Structures On Medium Angular Scales (COSMOSOMAS) experiment, with an observed polarization fraction at $\Pi = 3.4^{+1.5}_{-1.9}$ per cent that could be proceeding from AME. Other works employing different facilites only determined upper limits, usually in the range $\Pi \lesssim 1$–6 per cent (Casassus et al. 2008; Mason et al. 2009; Dickinson, Peel & Vidal 2011; López-Caraballo et al. 2011; Macellari et al. 2011; Battistelli et al. 2015). These constraints agree in the observed lack of a strong polarized AME component, but are still too loose to clearly discriminate between the different AME models.

This observational landscape emphasizes the need for accurate polarized sky surveys, in order to assess the foreground level of contamination to existing and future CMB observations. Polarized maps from the Wilkinson Microwave Anisotropy Probe (*WMAP*; Kogut et al. 2007) and *Planck* (Planck Collaboration VI 2020b) have been used to derive dust and synchrotron polarized sky models over frequencies ranging from 22.7 to 353 GHz (Krachmalnicoff et al. 2016). Ground-based facilities are capable of complementing this range with observations in the lower frequency portion of the microwave spectrum; for instance, the Cosmology Large Angular Scale Surveyor (CLASS) is designed to observe at 40, 90, 150, and 220 GHz (Watts et al. 2015), while the C-Band All Sky Survey (C-BASS; Irfan et al. 2015) is currently mapping the full sky at 5 GHz. This work focusses on data from the multifrequency instrument (MFI), the first instrument of the Q-U-I JOint TEnerife (QUIJOTE) experiment (Rubiño-Martín et al. 2017), spanning the frequency range from 10 to 20 GHz. QUIJOTE-MFI data have already been used to characterize polarized foregrounds; Génova-Santos, Rubiño-Martín & Rebolo (2015b) provided the constraints $\Pi < 10.1$ per cent at 12 GHz and $\Pi < 3.4$ per cent at 18 GHz for the AME polarization fraction (95 per cent C.L.), using QUIJOTE data in combination with ancillary observations towards the Perseus molecular complex. A similar study conducted over the W43 molecular complex provided the tightest constraints on AME polarization to date, $\Pi < 0.39$ per cent at 17 GHz and $\Pi < 0.22$ per cent at 41 GHz (95 per cent C.L.); these results are reported in Génova-Santos et al. (2017) together with the detection of AME in total intensity towards the molecular complex W47 and the modelling of the synchrotron polarized emission from the SNR W44. QUIJOTE data were also employed in Poidevin et al. (2019) for the characterization of AME towards the Taurus molecular cloud and the L1527 dark cloud nebula, enabling us to set upper limits for the polarized fraction at $\Pi <$

[1]Strictly speaking, the emission from one accelerated charge is intrinsically polarized; the observed free–free foreground, however, is generated by the superposition of the emissions from a population of electrons with random velocity directions, which erases the overall polarization fraction.

Downloaded from https://academic.oup.com/mnras/article/519/3/3432/6984761 by guest on 18 July 2023

3.8 per cent and $\Pi < 4.5$ per cent (95 per cent C.L.) respectively at 28.4 GHz. Finally, Cepeda-Arroita et al. (2021) combined QUIJOTE and C-BASS data to study the morphology of AME emission in total intensity towards the λ Orionis ring. As confirmed by these results, data already acquired by QUIJOTE represent a valuable addition to existing radio and microwave surveys when modelling both polarized and non-polarized foregrounds.

This work, the fifth in the series of QUIJOTE scientific papers, aims at characterizing in intensity and polarization the emission towards three Galactic regions: the SNRs with associated molecular clouds W49 and W51, and the SNR IC443. The goal is to provide a characterization of the local synchrotron emission (in particular of its spectral index), and to investigate AME intensity and possible polarization towards SNRs. This work is then intended as a continuation of the studies presented in Génova-Santos et al. (2015b), Génova-Santos et al. (2017) and Poidevin et al. (2019), dedicated to the characterization of astrophysically relevant Galactic regions using QUIJOTE data.

This paper is outlined as follows. In Section 2 we describe the Galactic regions we consider for our study. Section 3 presents the new data obtained with the QUIJOTE experiment, describing the observations and discussing the resulting maps. In Section 4 we detail the ancillary data set that we employ in our analysis. Section 5 is dedicated to the measurement of the relevant quantities associated with the intensity and polarized emission proceeding from the three regions, while in Section 6 we discuss the modelling and physical interpretation of these findings in terms of the known foreground emission mechanisms. Finally, Section 7 presents the conclusions.

2 THE GALACTIC REGIONS W49, W51, AND IC443

We dedicate this section to a description of the three Galactic regions considered in this work. W49 and W51 are the first important complexes encountered east of the W47 region that was studied in the second QUIJOTE scientific paper (Génova-Santos et al. 2017). Both these regions host SNRs; it is then interesting to combine their analysis with IC443, which is a relatively more isolated SNR. This allows us to assess the influence of molecular clouds and star forming regions on the AME signal towards SNRs. The position on the sky of these three sources is shown in Fig. 1, while in Table 1 we report a summary of their relevant information.

2.1 W49

W49 is a Galactic radio source discovered in the 22 cm survey of Westerhout (1958); it is located in *Aquila* on the plane of the Milky Way at Galactic coordinates[2] $(l_{\rm eff}, b_{\rm eff}) = (43.2^\circ, -0.1^\circ)$, with an angular size of ∼30 arcmin. The radio emission from this region can be separated into a thermal component designated W49A, centred at $(l, b) = (43.17^\circ, 0.00^\circ)$, and a non-thermal component labelled W49B, located at $(l, b) = (43.27^\circ, -0.19^\circ)$; this composite structure of W49 soon became evident from the results of high angular resolution continuum observations in the radio domain (Mezger, Schraml & Terzian 1967).

W49A (G43.2+0.0) is one of the largest and most active sites of star formation in our Galaxy; it is embedded in a giant molecular cloud of estimated mass $10^6\,{\rm M}_\odot$ over a total extension of 100 pc (Sievers et al. 1991; Simon et al. 2001; Galván-Madrid et al. 2013). Star formation is concentrated in a central region of ∼ 20 pc extension, which hosts several ultracompact H II (UCH II) regions. The W49A stellar population has been extensively studied using infrared (IR) observations (Wu et al. 2016; Eden et al. 2018), while observations in the radio domain have contributed to map the complex kinematics of the local gas (Brogan & Troland 2001; Roberts et al. 2011; Galván-Madrid et al. 2013; De Pree et al. 2018; Rugel et al. 2019; De Pree et al. 2020); high-energy γ-ray emission towards the region has also been detected (Brun et al. 2011). From the proper motion of H_2O masers, Gwinn, Moran & Reid (1992) estimated the distance of this region from the Sun at 11.4 ± 1.2 kpc, which was later refined by Zhang et al. (2013) as $11.11^{+0.79}_{-0.69}$ kpc. Because of its large distance, the region is optically obscured by intervening interstellar dust, which accounts for the lack of W49 optical observations. Given its total extension and gas mass, W49A is comparable to extra-Galactic giant star-forming regions, and as such it is the ideal environment to study massive star formation in starburst clusters, and the early evolution of H II regions (Wu et al. 2016; De Pree et al. 2018).

W49B (G43.3-0.2) is a young SNR which has also been extensively studied in the literature with observational data at different wavelengths. Pye et al. (1984) compared X-ray and radio observations of the region, revealing an anticorrelation between the corresponding morphologies: while the X-ray brightness profile is centrally peaked, the radio image is typical of a shell-like remnant with no indication of a central energy source. This morphology was confirmed by later studies (Rho & Petre 1998; Hwang, Petre & Hughes 2000; Keohane et al. 2007) and ascribed to a jet-driven supernova triggered by the collapse of a supermassive Wolf–Rayet star, with subsequent interaction with the circumstellar medium (Lopez et al. 2013; González-Casanova et al. 2014; Siegel et al. 2020). The supernova event occurred in between 1 and 4 kyr ago (Hwang et al. 2000; Zhou et al. 2011); the distance of W49B from the Sun was set at

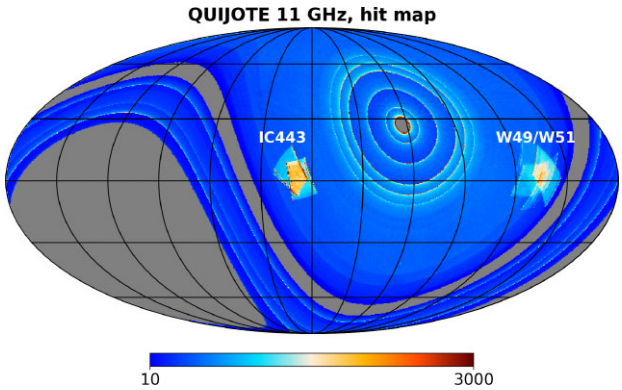

Figure 1. Map showing the number of hits per pixel (i.e. the number of 40 ms samples in each $N_{\rm side} = 512$ pixel) for the combined wide survey and raster scan data set (see Section 3.2 for details). The inclusion of raster scans determines a local increase in sensitivity towards the IC443 region and the area surrounding W49 and W51. The map is centred at Galactic coordinates $(l, b) = (180^\circ, 0^\circ)$ to better display the source areas. This map is obtained using 11 GHz data in total intensity, but the hit maps for the other frequency bands are qualitatively similar.

[2]Nominal coordinates quoted in the text are taken from the SIMBAD Astronomical Data base at http://simbad.u-strasbg.fr/simbad/. However, due to the extended nature of these sources, the SIMBAD coordinates are often representative only of specific subregions. The mean coordinates for the full regions were assessed considering studies in the literature at different wavelengths; in such cases, coordinates are labelled with the subscript 'eff', to stress that they mark an effective central position.

Downloaded from https://academic.oup.com/mnras/article/519/3/3432/6984761 by guest on 18 July 2023

Table 1. Summary of the three sources considered in this study. For each one we report the effective central Galactic coordinates (l_c, b_c), the possible substructures, the diametral angular size, the estimated distance and the age of the associated SNR. The last three columns quote the relevant quantities for the aperture photometry analysis described in Section 5, namely the radii of the chosen aperture (r_{ap}) and of the internal (r_{int}) and external (r_{ext}) boundaries of the background annulus.

Source	(l_c, b_c) (deg)	Substructures	Size (arcmin)	Distance (kpc)	SNR age (kyr)	r_{ap} (arcmin)	r_{int} (arcmin)	r_{ext} (arcmin)
W49	(43.20, −0.10)	W49A (thermal), W49B (SNR)	30	∼11	1–4	60	80	100
W51	(49.20, −0.35)	W51A, W51B (thermal), W51C (SNR)	50	∼5	30	80	100	120
IC443	(189.06, 3.24)	–	45	∼2	3–30	70	90	110

∼ 8 kpc by Moffett & Reynolds (1994). However, radio observations by Brogan & Troland (2001) pointed out that the morphology of H I gas towards the southern edge of W49B suggests interaction with the nearby W49A molecular cloud, thus allowing for a distance range of 8 to 12 kpc. By using a combination of radio and IR data, Zhu, Tian & Zuo (2014) later suggested a distance of ∼ 10 kpc; in contrast, observations of H_2 emission lines pointed again towards a shorter distance of 7.5 kpc (Lee, Koo & Lee 2020). The more recent analysis presented in Sano et al. (2021), based on the observation of CO emission lines, finally favours the value 11.0 ± 0.4 kpc, ascribing the smaller value obtained with H_2 to the latter tracing only a small portion of the associated molecular cloud; as the H_2 is thermally shocked and accelerated, distance measurements based on its velocity are likely biased. Finally, emission in γ rays proceeding from W49B has also been observed (Brun et al. 2011; H. E. S. S. Collaboration 2018), confirming the nature of an SNR interacting with molecular clouds.

W49 was considered as a possible candidate for AME in Planck Collaboration XV (2014a), where an emission excess was indeed found at typical AME frequencies. However, W49 was finally discarded from the list of significant AME sources due to the presence of local UCH II regions, which could contribute to the observed excess.

2.2 W51

The W51 region is located on the Galactic plane east of W49, at central coordinates (l_{eff}, b_{eff}) = (49.20°, −0.35°). It was also initially discovered in Westerhout (1958) radio survey, as another bright source in *Aquila*, and initially classified as an H II region. Subsequent radio observations identified the source as a molecular cloud (Penzias, Jefferts & Wilson 1971) and allowed us to further separate the region into three main substructures (Kundu & Velusamy 1967; Mufson & Liszt 1979): W51A and W51B, responsible for the observed thermal emission, and a non-thermal component W51C (for a detailed review of W51 morphology see Ginsburg 2017).

W51A and W51B are located at Galactic coordinates (l, b) = (49.48°, −0.33°) and (l_{eff}, b_{eff}) = (49.1°, −0.3°), respectively; these regions are embedded in a giant molecular cloud of $M > 10^6\,M_\odot$ (Carpenter & Sanders 1998), with W51A the main star-forming component. W51A is one of the most studied regions of massive star formation in our Galaxy; its rich morphology allows us to distinguish two main components, named G49.5-0.4 and G49.4-0.3 (Wilson et al. 1970). These components are further resolved into several regions (Martin 1972; Mehringer 1994; Okumura et al. 2000), among which we can cite the protoclusters IRS1 and IRS2 (Ginsburg et al. 2016). Several hypercompact H II regions have also been detected with radio data (Ginsburg et al. 2020; Rivera-Soto et al. 2020). This complex structure, combined with the local richness in gas and dust content, makes this region the ideal environment to study high-mass star formation (Ginsburg et al. 2017; Saral et al. 2017; Goddi et al. 2020). Despite all the observational endeavours, however, W51A stellar population is likely not completely catalogued (Binder & Povich 2018); recent studies of W51A using IR observations can be found in Lim & De Buizer (2019) and Bik et al. (2019), who confirmed the complexity of the ongoing star formation processes. The region also shows a rich astrochemistry (Vastel et al. 2017; Watanabe et al. 2017), which has been the object of studies searching for pre-biotic molecules in star-forming regions (Rivilla et al. 2016, 2017; Jacob et al. 2021). The parallax distance to this molecular cloud has been estimated from maser observations as $d = 5.41^{+0.31}_{-0.28}$ kpc (Sato et al. 2010) and as $d = 5.1^{+2.9}_{-1.4}$ kpc (Xu et al. 2009), depending on the considered subregion; these estimates place W51 in the Carina-Sagittarius arm.

W51B appears as a filamentary structure populated by UCH II regions; however, unlike W51A, most of the star formation in W51B seems to have already taken place, as suggested by the lower fraction of dense gas (Ginsburg et al. 2015).

W51C is an extended source of non-thermal radio emission located west of W51A and mostly south of W51B at (l_{eff}, b_{eff}) = (49.2°, −0.7°), which has been identified as a SNR (Seward 1990) with an estimated age of 30 kyr (Koo, Kim & Seward 1995). This source has been extensively observed in radio wavelengths (Zhang et al. 2017; Ranasinghe & Leahy 2018), X-rays (Koo et al. 2005; Hanabata et al. 2013) and γ-rays (Abdo et al. 2009; Aleksić et al. 2012). The distance of this SNR was first placed at 4.1 kpc (Sato 1973); later, Koo et al. (1995) estimated the distance to be ∼ 6 kpc, although with a high uncertainty given that this result is based on the association of the SNR with a molecular cloud which may extend over 1.5 kpc. Observations of the H I 21-cm line in absorption led to an estimated distance of 4.3 kpc (Tian & Leahy 2013) which has been recently re-evaluated as 5.4 kpc (Ranasinghe & Leahy 2018). The latter result is dictated by the observed interaction between W51C and W51B (Koo & Moon 1997; Brogan et al. 2013), which constrains the SNR to be at the same distance as the other W51 H II regions.

Overall, W51 has a luminosity to mass ratio similar to W49 (Eden et al. 2018); it subtends a region with diameter ∼50 arcmin on the sky (Bik et al. 2019). The search for AME in the region has been tackled by Demetroullas et al. (2015), where it is shown that a spinning dust component is not required for a proper modelling of W51 intensity spectrum. To our knowledge, no clear evidence of AME emission towards W51 has been reported in the literature.

2.3 IC443

IC443 (*Index Catalogue 443*) is a SNR located in the constellation of *Gemini* at Galactic coordinates (l, b) = (189.06°, 3.24°); it is therefore found close to the Galactic anticentre, with a lower emission

Downloaded from https://academic.oup.com/mnras/article/519/3/3432/6984761 by guest on 18 July 2023

Table 2. Summary of the information on the QUIJOTE-MFI observations centred on each source; the last column reports the mean fractional wide survey (WS) time contribution to the final maps, computed with respect to the total time obtained combining the selected raster data with the nominal mode data. See 3.1 for more details.

Source	Observation type	Observing dates	Covered area	Total observing time	Selected time fraction (per cent)	WS time fraction (per cent)
W49	193 drift scans (73 min)	June–August 2015	616 deg^2	235.6 h	78	20
W51	170 drift scans (74 min)	October–December 2016	708 deg^2	209.1 h	73	20
IC443	552 raster scans (29 min)	October 2014 – June 2015	474 deg^2	269.1 h	66	21

from the neighbouring background compared to W49 and W51, which are much closer in projection to the Galactic bulge. This source has been extensively observed throughout the whole spectrum, including radio (Kundu & Velusamy 1972; Green 1986; Castelletti et al. 2011; Mitra, Green & Rao 2014; Planck Collaboration VII 2016c; Egron et al. 2016, 2017), optical (Fesen 1984; Ambrocio-Cruz et al. 2017), X-ray (Petre et al. 1988; Matsumura et al. 2017; Greco et al. 2018; Zhang et al. 2018; Hirayama et al. 2019) and γ-ray (Torres et al. 2003; Tavani et al. 2010) frequencies. IC443 angular size is $\sim 45'$ (Green 2014); the related supernova event occurred in between 3 (Petre et al. 1988) and 30 kyr ago (Olbert et al. 2001), with more recent estimates favouring $\sim$20 kyr (Lee et al. 2008). The distance to IC443 is still under debate; estimates range in between 0.7 and 1.5 kpc (Lozinskaya 1981; Fesen 1984), with the latter value being the most commonly used in the literature. A higher distance of 1.5–2 kpc has been proposed due to IC443 association with the H II region Sh2-249 (Gao et al. 2011; see also fig. 4 in this paper); a more recent estimate by Ambrocio-Cruz et al. (2017) locates IC443 at 1.9 kpc from the Sun.

At radio frequencies IC443 shows two roughly spherical subshells of synchrotron emission, with different centres and radii (Onić, Urošević & Leahy 2017); the region appears brighter in its north-eastern limb in equatorial coordinates. These shells traditionally define the boundary of IC443; a fainter and larger shell has been detected, but it is not clear whether it is a different SNR, nor if it is actually interacting with IC443 (Lee et al. 2008). Radio thermal emission towards the region has also been observed, and ascribed to *bremmstrahlung* (Onić et al. 2012). X-ray observations, instead, reveal a centrally filled profile, which makes IC443 a mixed-morphology or thermal-composite SNR (Rho & Petre 1998; Rajwade et al. 2016). IC443 evolution and observed structure is the result of the interaction between the SNR and different phases of the surrounding interstellar medium (Lee et al. 2008; Koo et al. 2020; Ritchey et al. 2020; Ustamujic et al. 2021), with observational evidence of interaction with molecular gas in the south-east and north-west (Su et al. 2014; Yoshiike et al. 2017) and with an atomic cloud in the north-east (Kokusho et al. 2013). Observations in γ-rays towards IC443 are relevant for the study of Galactic cosmic rays; in particular, γ-ray emission deriving from the decay of pions (the 'pion-decay bump') has been detected by Ackermann et al. (2013). These pions are produced in collisions between accelerated cosmic-ray protons and interstellar material, so that the detection of the pion bump provides a direct evidence for the occurrence of proton acceleration in SNRs (Huang et al. 2020).

Finally, IC443 has already been a target in the search for AME. Onić et al. (2017) analysed the radio and microwave spectrum of the region, reporting hints of AME detection and a bending of the synchrotron spectrum; however, they stressed that further data in the range 10 to 100 GHz are required to confirm these results. A similar conclusion was reached by Loru et al. (2019), who detected a clear bump in the range 20–70 GHz in IC443 intensity spectrum.

3 QUIJOTE DATA

We present in this work data acquired with the QUIJOTE experiment (Génova-Santos, Rubiño-Martín & Rebolo 2015a; Rubiño-Martín et al. 2017), a scientific collaboration aimed at characterizing the polarization of the CMB, and other Galactic and extra-Galactic physical processes, in the frequency range 10–40 GHz and at angular scales larger than 1 degree. QUIJOTE consists of two telescopes and three instruments, operating from the Teide Observatory (Tenerife, Spain), a site that provides optimal atmospheric conditions for CMB observations in the microwave range (Rubiño-Martín et al. 2012b).

The data used in this work were acquired with the QUIJOTE multifrequency instrument (MFI; Hoyland et al. 2012), which consists of four conical corrugated feedhorns, each feeding a novel cryogenic on-axis polar modulator that can be rotated in steps of 22.5°. The output from each horn consists of eight channels carrying different linear combinations of the radiation Stokes parameters, which in turn are separated by the subsequent data analysis pipeline. Horns 1 and 3 both observe at frequency bands centred at 11 and 13 GHz, whereas horns 2 and 4 both observe at frequency bands centred at 17 and 19 GHz, all with a 2 GHz bandwidth. The full width at half-maximum (FWHM) is equal to 52 arcmin for the two low-frequency horns and to 38 arcmin for the two high-frequency horns. Overall, the MFI provides eight different maps of the sky in intensity and polarization, and is primarily devoted to the characterization of the Galactic emission. A full description of the MFI data reduction pipeline and map-making is provided in Génova-Santos et al. (in preparation).

3.1 Observations

The analysis presented in this paper is based on the combination of different QUIJOTE observations. We first consider data from the MFI wide survey, which covers more than 25 000 deg^2 including most of the northern sky, and as such encompasses the three regions targeted in this study. Observations were performed at fixed elevation by letting the telescope spin continuously in azimuth, and took place between 2013 May and 2018 June for a total observing time of $\sim$ 9200 h. The removal of bad data performed by the pipeline yields an effective total time of $\sim$ 8500 h in intensity and in the range $\sim$ 4700 h to $\sim$ 6800 h in polarization, depending on the chosen horn; the resulting data were used to produce the QUIJOTE wide survey legacy maps. An extensive description of the MFI wide survey and its associated data products can be found in Rubiño-Martín et al. (2022). On top of this large scale survey, we also consider a set of dedicated raster scan observations focused on each region, which we describe in the following; we stress that the raster scan observations constitute the major source of data used in the current analysis. A summary of the related information is also reported in Table 2.

W49 was mapped in 193 dedicated observations performed between 2015 June and August; these observations were drift scans in which the telescope elevation was maintained fixed and the pointing

Downloaded from https://academic.oup.com/mnras/article/519/3/3432/6984761 by guest on 18 July 2023

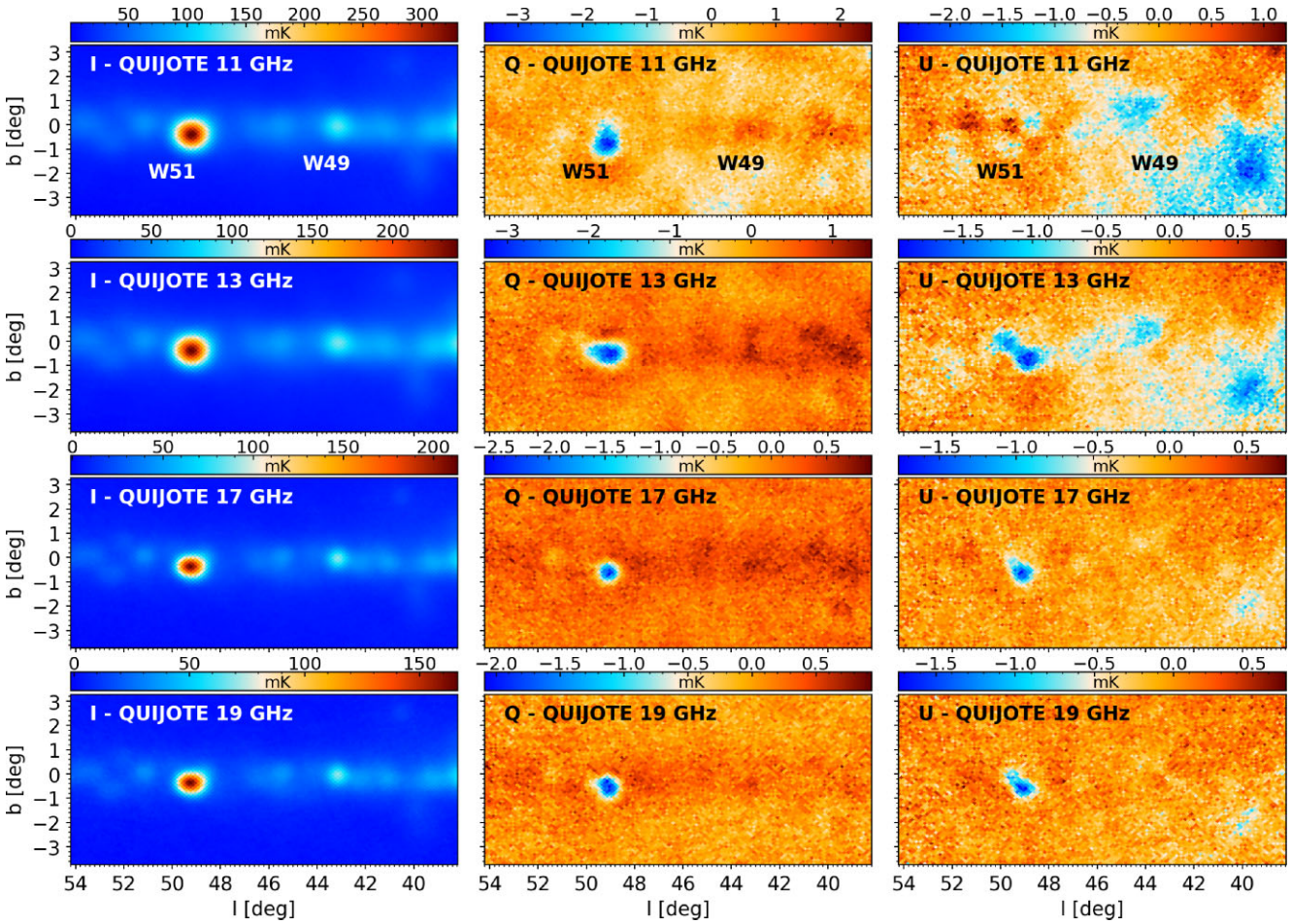

Figure 2. Intensity and polarization destriped maps of the sky region including the sources W49 and W51, for the four QUIJOTE frequencies. All maps are shown here at their original resolution.

was switched back and forth in azimuth with an ∼18/cos (EL) deg amplitude for each scan; each observation took on average 73 min, and covered a final mean area of 408 deg^2 per horn on the sky. Notice that the MFI focal plane configuration determines a different pointing for each horn for the same observation, with separations up to ∼5°; this extends the sky area covered by W49 rasters to 616 deg^2. The total observing time is 235.6 h; after the inspection and removal of bad data, which is performed for each horn independently,[3] the effective observing times for the four horns are 171.4, 194.1, 177.0, and 189.5 h, corresponding to a an average of ∼ 78 per cent of the total. After combining the good raster data with the nominal mode data, the latter account for 13.4 per cent, 29.0 per cent, 19.0 per cent, and 19.8 per cent of the total observing time in each horn; on average, the wide survey fractional time contribution to the final maps in the W49 region is ∼ 20 per cent.

W51 is located ∼ 6 deg east of W49 on the Galactic plane, so it was also captured by the drift scans we just described. However, due to the different horn sky coverage, W51 was only partially mapped in several observations. For this reason it was decided to perform an independent set of observations centred on W51: they were conducted between 2016 October and December, as a set of 170 fixed-elevation scans with a ∼20/cos (EL) deg azimuth amplitude, each lasting 74 min on average. The total observing time is 209.1 h, which after the good data selection amounts to 140.9, 152.7, 158.8, and 155.3 h for the four horns, corresponding to an average of ∼ 73 per cent of the total time. In this case, the nominal mode data contribute for 14.7 per cent, 21.3 per cent, 25.7 per cent, and 17.3 per cent of the total observing time in each horn after combination with raster data; again, the mean wide survey time contribution to the final maps is ∼ 20 per cent. Each horn covers on average 534 deg^2 on the sky, for a total 708 deg^2 mapped by the MFI with this set of observations. The overall sky area covered by the joint set of observations of W49 and W51 amounts to 891 deg^2, thus enabling an extended reconstruction of the Galactic plane region surrounding the two molecular complexes.

Finally, IC443 was targeted by 552 observations conducted between 2014 October and 2015 June. In this case the observations consisted in raster scans with an amplitude of ∼12/cos (EL) deg in azimuth, with the telescope being stepped ∼0.1 deg in elevation at the end of each scan, over a total ∼12 deg range. Each observation lasted 29 min on average, for a total observing time of 269.2 h. The selection of good data yielded 174.3, 192.8, 187.6, and 159.5 h for the four horns, averaging at ∼ 66 per cent of the overall dedicated time.

[3]Apart from the data flagging pipeline described in Génova-Santos et al. (in preparation), we also performed a visual inspection of local maps centred on each source. These maps were generated for each observation and each one of the 32 MFI channels, and were used to discard observations where the local background was too noisy in at least one channel.

Downloaded from https://academic.oup.com/mnras/article/519/3/3432/6984761 by guest on 18 July 2023

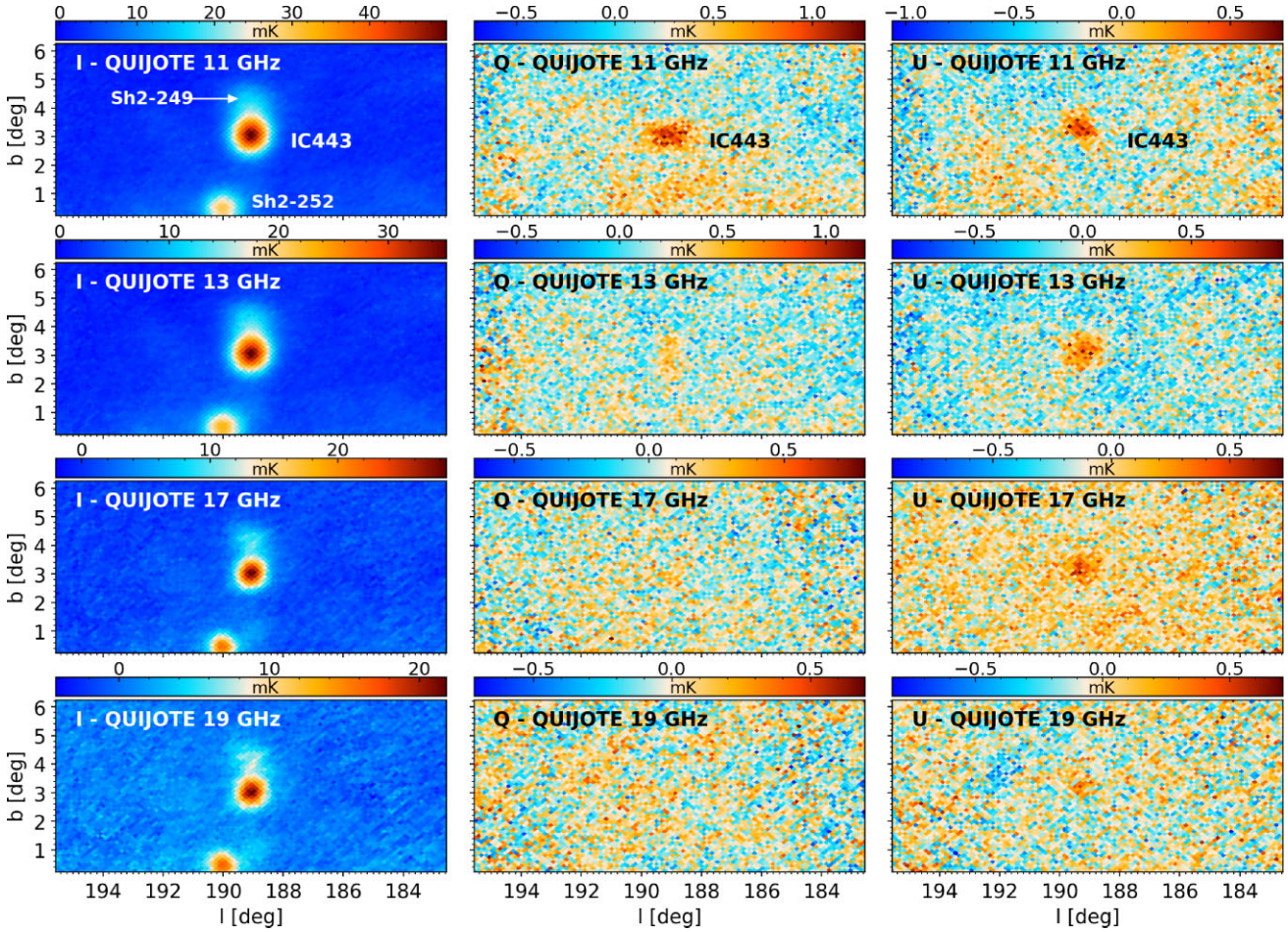

Figure 3. Same as in Fig. 2, but showing this time the IC443 region. The 11 GHz intensity map also marks the position of the two H II complexes surrounding the SNR.

Out of the combination with nominal mode data, the latter account for 10.2 per cent, 22.3 per cent, 24.0 per cent, and 27.9 per cent of each horn observing time, for an average time fraction of ~ 21 per cent. The mean area covered by each horn amounts to 360 deg^2, for a total 474 deg^2 mapped by the MFI in this region.

3.2 Maps

Time-ordered data from the raster scan observations are processed adopting the standard QUIJOTE pipeline described in Génova-Santos et al. (in preparation). Subsequently, these data are combined with data from the wide survey to produce the associated sky maps. The map-making is based on the PICASSO code (Guidi et al. 2021) with the same set of destriper parameters (noise priors and baseline length) adopted in Rubiño-Martín et al. (2022) when producing maps of the wide survey data alone. The resulting destriped map is provided using a HEALPIX pixelization (Górski et al. 2005) with $N_{\rm side} = 512$, corresponding to a 6.9 arcmin pixel size; this resolution is enough given that the MFI beam FWHM values are larger than 0.5°. The code provides full sky maps, with increased sensitivities towards the relevant regions thanks to the inclusion of raster scan data; this is visible in the hit map shown in Fig. 1, where we can clearly distinguish two regions with higher integration time, one centred on the Galactic plane around W49 and W51, and one centred on IC443. In the following we will focus on sub-maps centred on these specific areas. We remind that the wide survey maps presented in Rubiño-Martín et al. (2022) are corrected for residual radio frequency interference contamination by subtracting the median value of pixels in rings of constant declination (FDEC correction, see Section 2.4.2 in the aforementioned reference). However, as in this analysis we will only perform aperture photometry measurements (Section 5), this correction is unnecessary and is not applied to our combined wide survey plus raster scan maps. A quantitative estimation of the impact of FDEC on aperture photometry measurements is presented in appendix B1 in Rubiño-Martín et al. (2022), and is well below the uncertainties associated with our measurements presented in Section 5.

Local maps for W49/W51 and IC443 are plotted in Fig. 2 and in Fig. 3 respectively, in the three Stokes parameters I, Q and U, for the four MFI frequencies. Although in our subsequent analysis we will consider all maps smoothed to a common resolution of 1 deg, these plots show the maps in their original resolution. As two horns cover each frequency band, their individual maps are combined to yield the final map of the corresponding band. However, for the low frequency bands (11 and 13 GHz) the maps we employ are the ones obtained from horn 3 data alone; this is due to a fault in the polar modulator of horn 1, which has been fixed to the same position since 2012 September, thus making data obtained with this horn not reliable.[4] For the case of 17 and 19 GHz, instead, the maps we show are obtained from a linear combination of horn 2 and horn 4 maps,

[4]Although we discard horn 1 data in this paper analysis, its maps in total intensity were none the less generated using the standard pipeline; hence,

Downloaded from https://academic.oup.com/mnras/article/519/3/3432/6984761 by guest on 18 July 2023

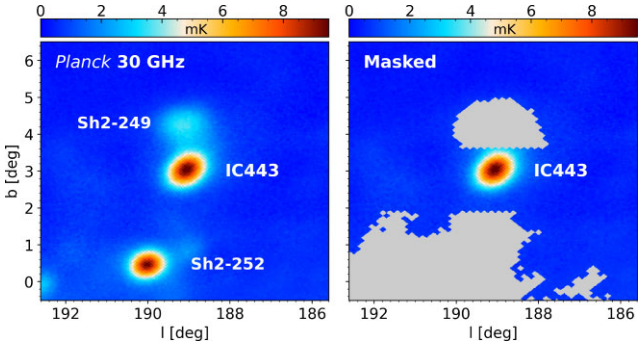

Figure 4. Left-hand panel: The area surrounding IC443 shown on the *Planck* 30 GHz total intensity map (2015 data release). Right-hand panel: The same area after applying a tailored mask which excises the contribution from the H II regions Sh2-249 and Sh2-252.

each weighted by a uniform weight computed from the white noise in the power spectrum of the associated wide survey map (for details see Rubiño-Martín et al. 2022).

In Fig. 2 we show the QUIJOTE maps for the Galactic plane region encompassing the sources W49 and W51. The Galactic plane is easily recognizable in the intensity maps, as a stripe of diffuse emission surrounding the compact objects; this diffuse emission is also visible in polarization, with the expected[5] imprint of positive Q and nearly zero U. In intensity both W49 and W51 are clearly visible; at the western edge of the intensity maps it is possible to see the border of the source W47, which was studied in Génova-Santos et al. (2017). W51 appears particularly bright in these maps; it saturates the chosen colour scales in intensity, while in polarization it shows a clear emission with both negative Q and U, which makes it stand out from the diffuse Galactic plane polarization signal. As commented in Section 2.2, W51 size is ∼50 arcmin, which means it is partially resolved with QUIJOTE beams; indeed, a mismatch is visible between the centres of the intensity and polarization emissions, with Q and U peaks being slightly displaced towards the south-east. A possible explanation for this is that while the bulk of the intensity emission comes from the molecular cloud hosting W51A, the polarized emission is from the SNR W51C only. W49 appears fainter in intensity, and does not reveal a clear hint of polarized emission, although the diffuse Galactic plane polarization shows an increment in positive Q at the source position. Unlike W51, there is no particular internal structure visible for this source; its angular size of ∼30 arcmin implies it is not resolved by QUIJOTE.

IC443 maps are shown in Fig. 3. As commented in Section 2.3, the source is located towards the Galactic anticentre and at a Galactic latitude of ∼3°, therefore the Galactic plane emission is not visible in these maps; its outskirts, however, still enter the maps as a background emission gradient that increases towards the south. In addition, two radio sources are visible in the vicinity of IC443: a bright source towards the southeast, which we can identify as the HII region Sh2-252 (also referred to as NGC2174, Bonatto & Bica 2011) and a fainter feature just north of the SNR, which produces an apparent elongation of IC443 in that direction and can be ascribed to the H II region Sh2-249 (Dunham et al. 2010; Gao et al. 2011). The emission from these sources can affect the flux density estimates in this region; therefore, we apply to all IC443 maps an ad hoc mask built to block the contribution of the neighbouring objects. The details of the mask are visible in the right-hand panel of Fig. 4. In the QUIJOTE intensity maps the source is clearly detected, although the background at 19 GHz is noisier compared to the maps obtained for W49 and W51; in polarization the maps show a positive U emission and hints of a positive Q emission (with a more significant detection at 11 GHz) towards the source, which can be ascribed to synchrotron emission proceeding from the SNR.

3.3 Null-test maps and noise levels

We use a null test map built from QUIJOTE data to evaluate the contribution of instrumental noise. For each observed region, we split the available data in two halves with the same number of observations, in such a way that each half has a sky coverage as similar as possible as the other; for the wide survey data we use the same halves as in Rubiño-Martín et al. (2022). In order to allow a proper reconstruction of the polarized signal from each half, care is taken to split observations in such a way that the distribution of observations in each polar modulator position is the same in both halves. For each half we then generate the corresponding maps adopting the same processing pipeline that was used for the full data set. We then obtain the null-test maps as:

$$M_{\rm NT} = \frac{1}{2}\left(M_{\rm H1} - M_{\rm H2}\right), \tag{1}$$

where $M_{\rm H1}$ and $M_{\rm H2}$ represent the first and second half maps. By construction, the resulting map $M_{\rm NT}$ should be free from the sky signal, which cancels out in the subtraction, and be representative of the instrumental contribution only. We compute the instrumental noise component as the rms of the pixel values found in a 1-deg radius aperture on each null map. The resulting quantity represents the rms of individual pixels; to be consistent with other QUIJOTE works, we convert it into the rms of a Gaussian beam with FWHM = 1°, by dividing the original rms by the square root of the number of pixels entering the beam solid angle. We place our aperture far from the sources, centred at $(l, b) = (46°, -2°)$ for the W49/W51 map, and at $(l, b) = (186°, 2.5°)$ for the IC443 map; this choice allows us to compare this rms with the same quantity evaluated on the full data set maps. The two values of rms are directly comparable thanks to the factor 1/2 in equation (1), which cancels the $\sqrt{2}$ factor coming from the linear combination of the two half-maps, and the additional $\sqrt{2}$ factor coming from the splitting of the available statistics that increases the rms of each half-map. The comparison for the Stokes parameters I, Q, and U is reported in Table 3 for both the W49/W51 and the IC443 maps.

We see that in polarization the real maps and the null-test maps have similar rms values, which means that the main contribution to the polarization maps used in this study is noise. For intensity, instead, the rms is considerably higher when evaluated in the full data maps than in the null-test maps. This is indicative of an important contribution from the sky emission in the estimation of the noise. The effect is stronger for the W49/W51 map due to the proximity of the regions to the Galactic plane, which introduces gradients in the background signal. The polarization rms values quoted in Table 3 are about a factor 2 lower than the ones obtained from the wide survey maps only (Rubiño-Martín et al. 2022); this shows the improvement in the map quality achieved by including the dedicated

for completeness, we still included the description of its contribution to the acquired data in Section 3.1 and in Table 2.

[5]In this work we follow the HEALPIX definition of the Stokes parameters, usually referred to as the 'COSMO convention', which differs from the IAU convention in a sign flip of U.

Downloaded from https://academic.oup.com/mnras/article/519/3/3432/6984761 by guest on 18 July 2023

Table 3. Results of the null test performed on QUIJOTE maps. For each frequency and Stokes parameter we compare the 1-deg beam rms obtained in the original map (Map) and in the null test map (NT). The last column reports the resulting MFI instantaneous sensitivity in polarization.

Frequency (GHz)	σ_I (μK beam^{-1}) Map	NT	σ_Q (μK beam^{-1}) Map	NT	σ_U (μK beam^{-1}) Map	NT	$\sigma_{Q,U}$ (mK s$^{1/2}$) NT
			W49/W51				
11.0	617.4	53.8	25.8	22.5	21.9	21.3	1.4
13.0	489.8	34.6	18.9	16.2	15.9	15.1	1.2
17.0	300.7	57.5	14.1	13.1	13.8	13.2	1.4
19.0	252.9	71.7	15.9	12.8	15.3	14.6	1.4
			IC443				
11.0	71.1	59.8	21.2	19.6	21.1	20.0	1.1
13.0	52.2	44.7	20.1	18.4	18.4	19.0	1.0
17.0	80.9	62.4	16.0	15.3	19.2	15.8	1.2
19.0	100.1	79.3	18.8	17.6	19.2	17.1	1.4

raster scan observations towards our sources. In fact, the sensitivity in polarization averages around ~ 15 μK beam^{-1}, which is the deepest level reached by published QUIJOTE data so far.

The last column in Table 3 reports the instantaneous sensitivity of the maps in polarization, computed by multiplying the quoted Q and U rms values per beam by the square root of the mean observing time per 1-deg beam; the results for Q and U are then averaged (in quadrature) to yield the values of $\sigma_{Q,U}$ reported in the table. In general, these estimates range from 1.0 to 1.4 mK s$^{1/2}$; this is expected, since the nominal instrument sensitivity in polarization is ~ 1 mK s$^{1/2}$. Our findings are consistent with previously reported values for the instantaneous sensitivity (Génova-Santos et al. 2015b, 2017). This test confirms the good quality of the polarization maps, and that the instrumental noise contribution to the maps is controlled and within the expected limits.

4 ANCILLARY DATA

In order to better characterize the emission from the Galactic regions considered in this study, we also employ ancillary data that extend the information provided by QUIJOTE observations to both lower and higher frequencies. We use all maps in a common HEALPIX pixelization of $N_{\rm side} = 512$, and at a common angular resolution of 1 deg. With the exception of *WMAP* maps, which are already available at this angular resolution at the LAMBDA website,[6] in all the other cases the smoothed maps are obtained by deconvolving the original beam (the nominal survey FWHM was used in each case and a Gaussian beam shape was assumed) and convolving with a 1 deg FWHM Gaussian beam. QUIJOTE maps are also degraded to this coarser resolution for the photometric analysis. The relevant properties of all the ancillary maps used in this study are summarized in Table 4.

4.1 Lower frequency ancillary data

In the radio and microwave domains, we consider the map at 408 MHz from Haslam et al. (1982) survey, which covers the whole sky with observations from different facilities (Jodrell Bank MkI and MkIA-76 m, Bonn-100 m, and Parkes-64 m telescopes), the Berkhuijsen (1972) map at 820 MHz, obtained from a survey with the Dwingeloo-25 m telescope, the Reich & Reich (1986) survey at 1420 MHz conducted with the Stockert-25 m and the Villa-Elisa-30 m telescopes, and the Jonas et al. (1998) survey at 2326 MHz obtained with the HartRAO-26 m telescope.

We actually use the 408, 1420, and 2326 MHz maps provided by Platania et al. (2003), which are corrected for the artefacts produced by observational strategy and instrumental gain drifts; the 820 MHz map is instead generated by projecting into HEALPIX pixelization the corresponding observational data retrieved from the MPIfR's Survey Sampler.[7] These radio maps only provide intensity data and are calibrated referring to the full-beam solid angle; as explained in Reich & Reich (1988), the sidelobe contribution would lead to an underestimation of the flux density for sources which are small compared to the main beam. This effect is particularly important for the Reich & Reich (1986) survey, and in the aforementioned reference it is argued that a correction factor of 1.55 can be used to account for the flux density loss. Since the FWHM for the Stockert telescope is ~35 arcmin, this factor can be applied for W49, but not for W51 and IC443, whose angular sizes are larger than the survey beam; in these cases, we employed a more conservative value of 1.25. These multiplicative factors are employed to correct the flux densities extracted from the 1420 MHz map in the aperture photometry analysis described in Section 5. Although a similar issue affects the 2326 MHz map, we do not apply any explicit correction as the HartRAO beam is considerably smaller (20 arcmin) than the size of our sources. It is worth mentioning that the HartRAO map, which we use for the total intensity signal, actually carries the combination $I + Q$, and can consequently yield biased estimates of I flux densities towards polarized regions. However, as it is clear from the photometric analysis results in section 5, the polarized flux density is typically < 2 per cent of the flux density in total intensity, and the conservative 10 per cent calibration uncertainty adopted for the HartRAO measurement (see again Section 5) is enough to account for this bias.

In polarization we consider the survey carried out by the Dominion Radio Astronomy Observatory (DRAO; Wolleben et al. 2006), which provides Stokes Q and U maps for the northern sky at 1.41 GHz. We stress that the DRAO maps are delivered[7] following the IAU convention for the definition of the Stokes parameters; hence, we adapt it to the convention chosen in this work by flipping the sign of the U map. Finally, we employ the intensity and polarization maps

[6]Legacy Archive for Microwave Background Data Analysis, http://lambda.gsfc.nasa.gov/.

[7]http://www3.mpifr-bonn.mpg.de/survey.html.

Downloaded from https://academic.oup.com/mnras/article/519/3/3432/6984761 by guest on 18 July 2023

Table 4. Summary of the ancillary data detailed in Section 4, which are used in combination with QUIJOTE data to broaden the considered frequency range. For each map we report the frequency, the reference telescope(s) or satellite, which Stokes parameters are available, the original map resolution and units, the applied calibration uncertainty and the reference in the literature.

Frequency (GHz)	Facility	Stokes	Original resolution (arcmin)	Original units	Calibration uncertainty (per cent)	Reference
0.408	Jodrell Bank MkI, MkIA-76 m, Bonn-100 m, Parkes-64 m	*I*	51	K	10	Haslam et al. (1982), Platania et al. (2003)
0.820	Dwingeloo-25 m	*I*	72	K	10	Berkhuijsen (1972)
1.410	DRAO-25.6 m	*Q*, *U*	36	mK	10	Wolleben et al. (2006)
1.420	Stockert-25 m, Villa-Elisa-30 m	*I*	36	K	10	Reich & Reich (1986), Platania et al. (2003)
2.326	HartRAO-26 m	*I*	20	K	10	Jonas, Baart & Nicolson (1998), Platania et al. (2003)
4.800	Urumqi-25 m	*I*, *Q*, *U*	9.5	mK	10	Gao et al. (2010), Sun et al. (2011)
22.8	*WMAP* 9-yr	*I*, *Q*, *U*	50.7	mK	3	Bennett et al. (2013)
28.4	*Planck*-LFI	*I*, *Q*, *U*	32.29	K	3	Planck Collaboration XVI (2016b), Planck Collaboration VI (2020d)
33.0	*WMAP* 9-yr	*I*, *Q*, *U*	38.8	mK	3	Bennett et al. (2013)
40.6	*WMAP* 9-yr	*I*, *Q*, *U*	30.6	mK	3	Bennett et al. (2013)
44.1	*Planck*-LFI	*I*, *Q*, *U*	27.00	K	3	Planck Collaboration XVI (2016b), Planck Collaboration VI (2020b)
60.8	*WMAP* 9-yr	*I*, *Q*, *U*	20.9	mK	3	Bennett et al. (2013)
70.4	*Planck*-LFI	*I*, *Q*, *U*	13.21	K	3	Planck Collaboration XVI (2016b), Planck Collaboration VI (2020b)
93.5	*WMAP* 9-yr	*I*, *Q*, *U*	14.8	mK	3	Bennett et al. (2013)
100	*Planck*-HFI	*I*, *Q*, *U*	9.68	K	3	Planck Collaboration XVI (2016b), Planck Collaboration VI (2020b)
143	*Planck*-HFI	*I*, *Q*, *U*	7.30	K	3	Planck Collaboration XVI (2016b), Planck Collaboration VI (2020b)
217	*Planck*-HFI	*I*, *Q*, *U*	5.02	K	3	Planck Collaboration XVI (2016b), Planck Collaboration VI (2020b)
353	*Planck*-HFI	*I*, *Q*, *U*	4.94	K	3	Planck Collaboration XVI (2016b), Planck Collaboration VI (2020b)
545	*Planck*-HFI	*I*	4.83	MJy sr^{-1}	6.1	Planck Collaboration XVI (2016b)
857	*Planck*-HFI	*I*	4.64	MJy sr^{-1}	6.4	Planck Collaboration XVI (2016b)
1249	*COBE*-DIRBE	*I*	37.1	MJy sr^{-1}	11.9	Hauser et al. (1998)
2141	*COBE*-DIRBE	*I*	38.0	MJy sr^{-1}	11.9	Hauser et al. (1998)
2998	*COBE*-DIRBE	*I*	38.6	MJy sr^{-1}	11.9	Hauser et al. (1998)

from the Sino-German 6 cm survey of the Galactic plane (Gao et al. 2010; Sun et al. 2011), conducted with the Urumqi-25 m telescope at 4.8 GHz.[8]

4.2 Higher frequency ancillary data

In the microwave and far-infrared (FIR) range we employ data from the CMB satellite missions *WMAP*, *Planck*, and *COBE*. We consider the five *WMAP* bands at 23, 33, 41, 61, and 94 GHz, using the corresponding maps in the Stokes parameters *I*, *Q*, and *U* from the 9-yr *WMAP* data release (Bennett et al. 2013), available at the LAMBDA data base.

As for the *Planck* data, we use the maps from the second data release (Planck Collaboration XIII 2016b), which are publicly available at the *Planck* Legacy Archive (PLA) webpage.[9] The website provides the nine individual frequency survey maps in intensity, at 30, 44 and 70 GHz from the Low Frequency Instrument (LFI), and at 100, 143, 217, 353, 545 and 857 GHz from the high frequency instrument (HFI). The 100, 217 and 353 maps are contaminated by the CO rotational transition lines (1–0), (2–1) and (3–2), respectively, so these maps were first corrected using the *Planck*-released Type 1 CO maps (Planck Collaboration XVI 2014a), also available in the PLA webpage. In polarization, instead, we use the available maps up to 353 GHz from the third data release (Planck Collaboration VI 2020b), whose main improvement with respect to the second data release is precisely in the polarization data. Since after a visual inspection of the maps we detected artefacts affecting the 30 GHz *U* map towards W51, just for this frequency we adopt instead the polarization maps obtained from the NPIPE pipeline (Planck Collaboration VI 2020d).

Finally, we use the Zodi-Subtracted Mission Average maps from the DIRBE instrument on the *COBE* mission (Hauser et al. 1998) at 1249, 2141 and 2998 GHz; these maps are available in HEALPIX format at the CADE data base.[10] Maps for these frequencies are in total intensity only.

[8] http://zmtt.bao.ac.cn/6cm/surveydata.html.
[9] https://pla.esac.esa.int/#home.
[10] *Centre d'Analyse de Données Etendues*, http://cade.irap.omp.eu/dokuwiki/doku.php?id = dirbe.

Downloaded from https://academic.oup.com/mnras/article/519/3/3432/6984761 by guest on 18 July 2023

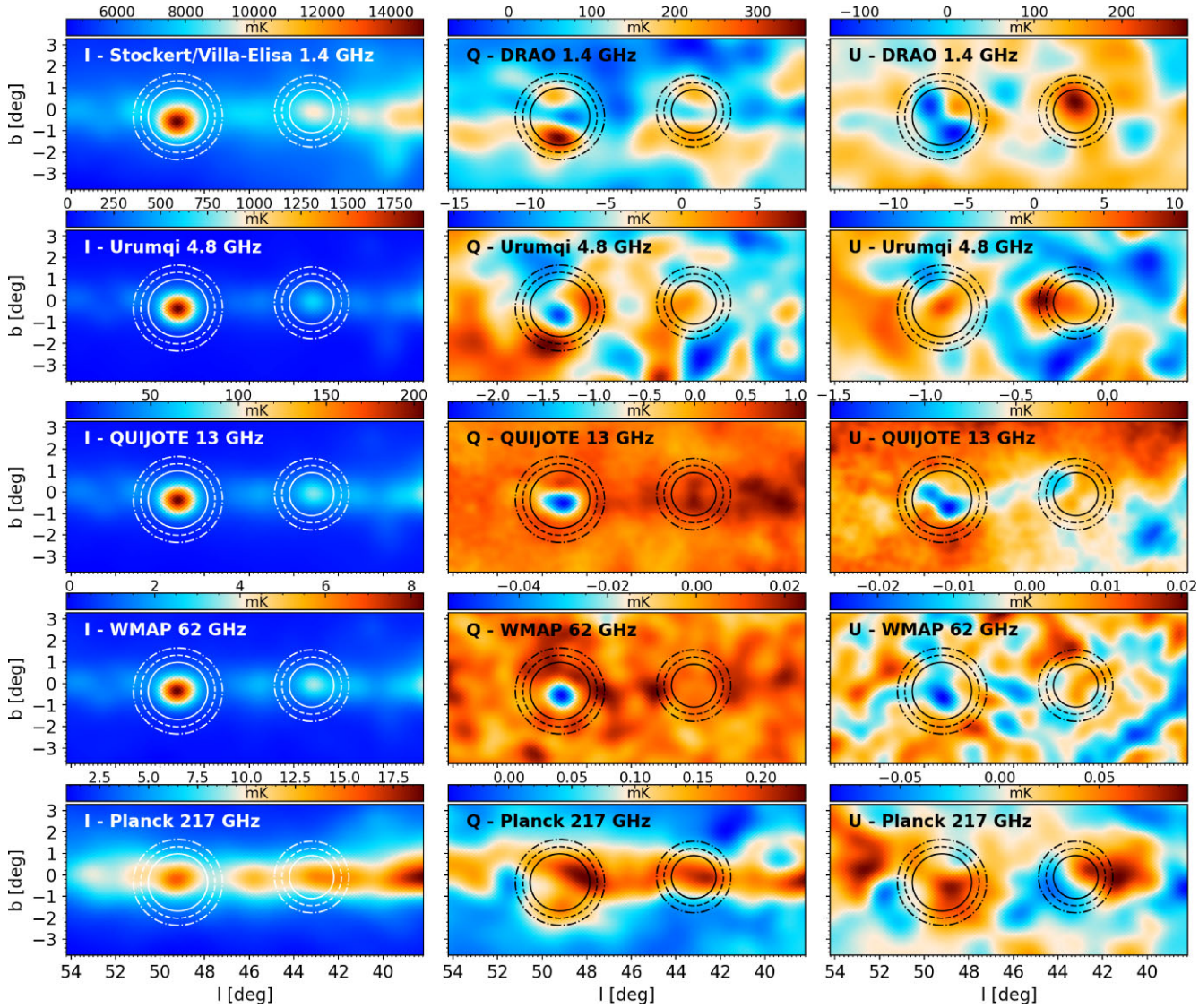

Figure 5. Sample intensity and polarization maps of the sky region including the sources W49 and W51, degraded to a 1 deg resolution, across the frequency range employed for the SED study. The apertures and background annuli used for the aperture photometry analysis are overplotted to each panel.

5 SED OF SOURCES

The characterization of the emission from our sources is primarily achieved by analysing their spectral energy distribution (SED), i.e. the frequency dependence of the observed flux densities in intensity and polarization. Flux densities are measured with the aperture photometry technique, following the implementation described in Génova-Santos et al. (2015b) and also adopted by Génova-Santos et al. (2017) and Poidevin et al. (2019) for the study of other compact sources. Apart from the previous QUIJOTE studies, aperture photometry has already been exploited for SED reconstruction in previous works (Dickinson et al. 2011; Génova-Santos et al. 2011; López-Caraballo et al. 2011; Rubiño-Martín et al. 2012a; Demetroullas et al. 2015; Planck Collaboration XIII 2016c). The technique consists in estimating the mean map temperature inside a suitable aperture centred on the source, and in removing a background level estimated as the median signal within a surrounding annulus; the result is then converted into flux density using the analytical conversion factor between temperature units and Jy, and the angular size subtended by the aperture. The sizes of the aperture and annulus depend on the considered source. We adopt the values reported in Table 1 which suit the different angular extents of the three regions; the table also reports the reference source position onto which all circles are centred. This choice is adopted for all the QUIJOTE and ancillary maps smoothed to a 1 deg resolution, and for measuring both the intensity and polarization SEDs. The corresponding circles are overplotted to the intensity and polarization maps shown in Figs 5 and 6. Notice that although in other works the background is estimated as the mean value of map pixels in the annulus, in our case the regions are close to the Galactic plane, implying that strong signal variation on scales comparable to our apertures may bias the estimation of the background level. The choice of the median of the annulus pixels is then made to minimize this effect, as discussed in Rubiño-Martín et al. (2012a).

The uncertainties on the measured flux densities can be computed as explained in Génova-Santos et al. (2015b), by using the rms of the pixels located in the background annulus (which is not biased by the source emission) and considering the contribution from the number of independent pixels in the aperture and in the annulus. We found

Downloaded from https://academic.oup.com/mnras/article/519/3/3432/6984761 by guest on 18 July 2023

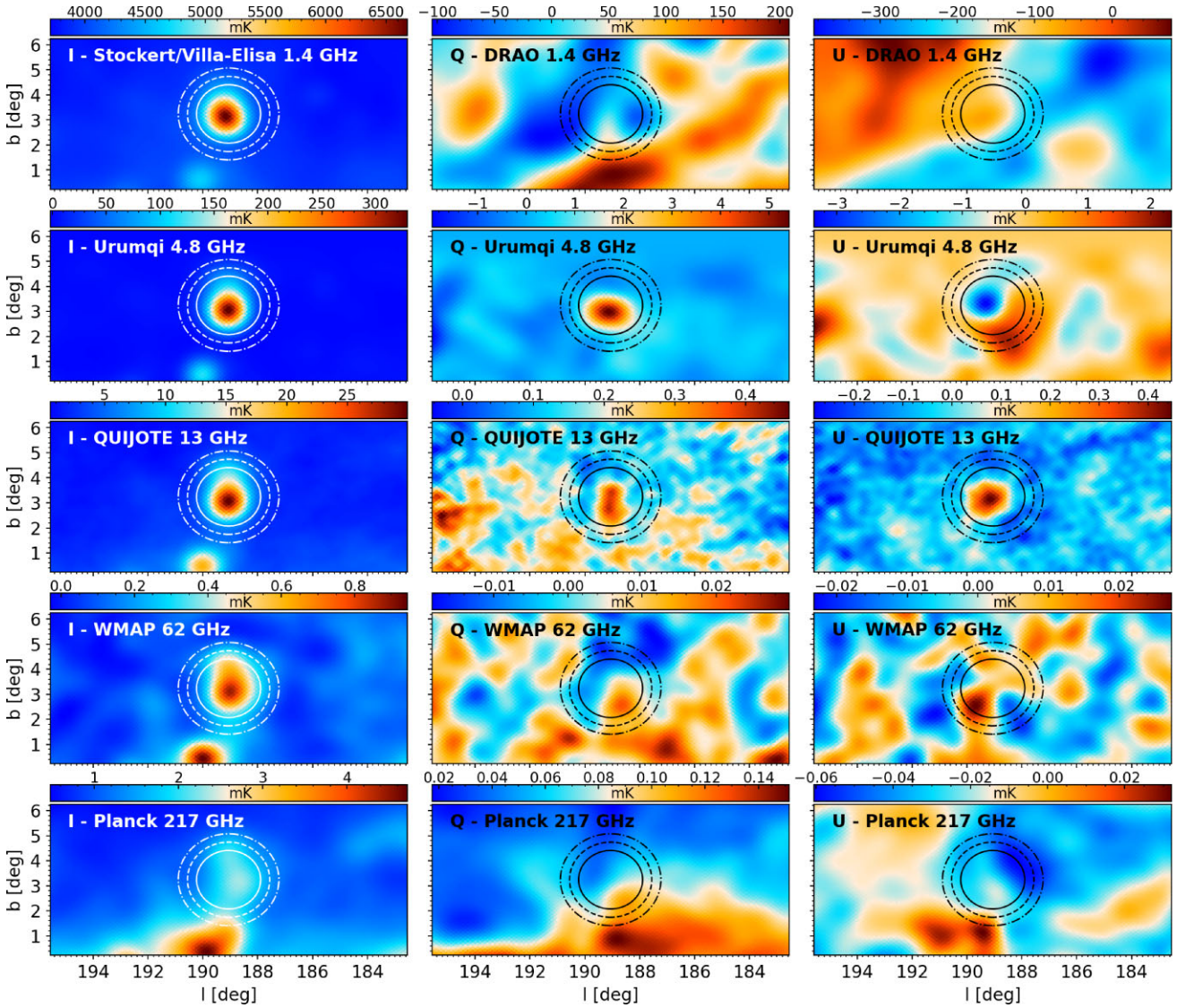

Figure 6. Same as in Fig. 5, but showing this time the IC443 region. The mask is not included to better show the evolution of the background with frequency.

that this method, although providing reasonable error estimates in total intensity, tends to underestimate the uncertainties in the Q and U flux densities. We then choose to compute the flux density errors, both in intensity and in polarization, as the rms of the flux densities computed in 10 apertures randomly located around the source, in such a way as to avoid the diffuse emission from the Galactic plane region and other intervening compact sources. The chosen apertures are shown in Fig. 7 for all three regions; the radii for the central aperture and the background annulus are the same as the ones employed for computing the source flux densities. These error estimates capture the typical fluctuations of the background at the aperture scale, and represent therefore a more reasonable estimate for the flux density uncertainties.

We also include a calibration error a posteriori, which is taken as a fixed fraction of the measured flux density and added in quadrature to the rms of the random apertures. This additional component is chosen to include all possible systematics affecting our flux density measurements. We adopt a conservative calibration error equal to 10 per cent of the flux density for all the low frequency points, from 408 MHz to 4.8 GHz; this choice is consistent with previous QUIJOTE studies, as in Génova-Santos et al. (2017) and Poidevin et al. (2019). Indeed, these points have a high statistical weight in the modelling of the source emission, since they anchor the total intensity level of synchrotron and free–free amplitudes at low frequencies, and as such affect the required level of AME in the microwave range. Similarly, the DRAO and Urumqi points are the only available low-frequency polarized flux densities, and their statistical weight is high in fixing the slope of the polarized synchrotron power law. However, these points are also affected by important systematic effects (for instance, the main-beam calibration issue described in Section 4.1), so that a significative calibration error is required to mitigate them. For the specific case of the Urumqi point we also consider an additional contribution to the error in the Q and U flux densities, taken as a fraction ($\sim$1 per cent) of the measured flux density in total intensity; this is done in view of the irregular trend shown by Urumqi polarized maps in Figs 5 and 6, in order to account for possible intensity-to-polarization leakages. Finally, following again a similar convention as in other QUIJOTE-MFI studies, we include conservative calibration uncertainties of 5 per cent for QUIJOTE points, 3 per cent for *WMAP* and *Planck* up to 353 GHz,

Downloaded from https://academic.oup.com/mnras/article/519/3/3432/6984761 by guest on 18 July 2023

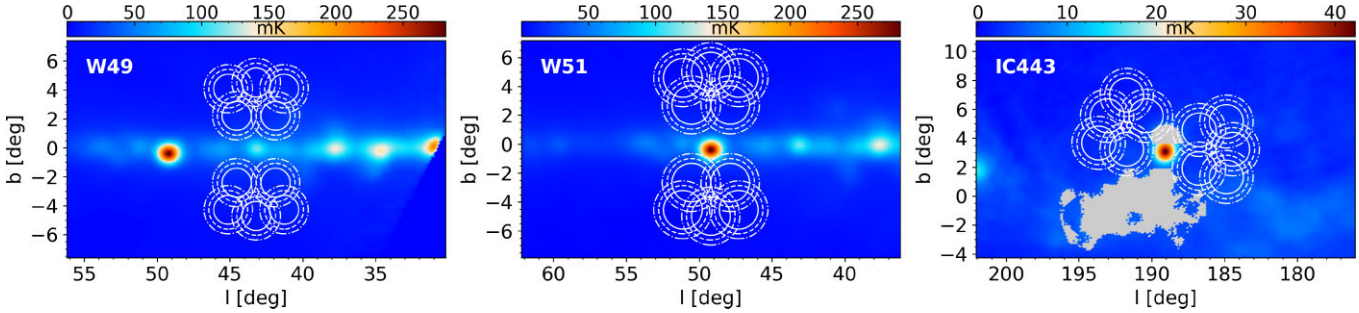

Figure 7. Random apertures employed to estimate the uncertainties on the source flux densities, overplotted for all three regions onto QUIJOTE 11 GHz total intensity maps smoothed to a 1 deg resolution. The IC443 tailored mask is also shown in the third panel. The size of the central apertures and the background annuli are the same as the ones used for measuring the source flux density.

6.1 per cent for 545 GHz, 6.4 per cent for 857 GHz and 11.9 per cent for DIRBE points (Planck Collaboration VIII 2011; Planck Collaboration XVI 2014a; Poidevin et al. 2019; Cepeda-Arroita et al. 2021).

Apart from the Stokes parameters Q and U, it is interesting to investigate the frequency dependence of the total polarized intensity P. The flux density for the latter can be evaluated as $P = (Q^2 + U^2)^{1/2}$, and the corresponding uncertainty σ_P is obtained by propagating the uncertainties σ_Q and σ_U on the Stokes parameters, measured on the corresponding maps. We also consider the polarization fraction, defined as $\Pi = P/I$, whose uncertainty is determined by propagating the errors on I and P. It is important to notice that these definitions of P and Π result in their posterior distributions being non-Gaussian; as detailed in Rubiño-Martín et al. (2012a), this may result in the final polarization estimates being positively biased, especially when the signal-to-noise ratio of the detection is low. Since studies of AME polarization generally quote upper limit on Π, this issue is particularly relevant in our analysis. Hence, we apply a debiasing correction according to the methodology described in Rubiño-Martín et al. (2012a), whereby the most likely value for the polarized flux density and fraction is obtained by integrating the posterior distributions on P and Π, respectively. The posterior distribution on P has been derived analytically in the literature (Vaillancourt 2006), and we adopt it to debias the polarization flux densities. For the case of Π, instead, the posterior is reconstructed with a Monte Carlo approach, by drawing random values for Q and U; values are sampled from a normal distribution whose width is given by the measured uncertainties on the Stokes parameters. The same approach was also adopted in Génova-Santos et al. (2017).

The measurements of the polarized Stokes parameters Q and U also allow us to estimate the polarization angle γ for the three regions at different frequencies. We adopt the definition $\gamma = -0.5 \arctan(U/Q)$, where it is understood that the arctangent is to be evaluated element-wise, taking into account the individual signs of Q and U, in order to have the final angle defined in $[-\pi/2, \pi/2]$. Although we adopt the HEALPIX convention for the sign of the Stokes parameters, this expression still ensures the angle is measured positive north through east.

Finally, we apply colour corrections (CC) to our flux density estimates, in order to account for the signal alteration due to the finite instrumental bandpass. This issue is particularly relevant for QUIJOTE, *WMAP*, *Planck*, and DIRBE, whereas for the lower frequency surveys the bandwidth is typically narrow enough to make this correction unnecessary. Information on the bandpasses for the aforementioned satellite-based data was retrieved from the LAMBDA and PLA archives, whereas for QUIJOTE the measured instrumental bandpasses were employed (see Génova-Santos et al., in preparation, for details). The CC computation requires the bandpass integration of a suitable model for the spectral dependence of the source flux density; for this we employ the model we fit on the data (Section 6) in an iterative procedure. The model initially fitted on the uncorrected flux densities is used to obtain a first CC estimation; these CCs are used to correct the initial flux densities and their uncertainties before repeating the fit. This procedure is repeated until convergence, which is always reached within the third iteration. The magnitude of the final colour corrections is typically $\lesssim 2$ per cent for QUIJOTE, $\lesssim 3$ per cent for *WMAP*, $\lesssim 1.5$ per cent for *Planck*-LFI, and $\lesssim 10$ per cent for *Planck*-HFI and DIRBE.

The final estimates for the parameters I, Q, U, P, Π and γ are reported in Tables 5, 6 and 7 for the regions W49, W51 and IC443, respectively. Notice that the 2326 MHz point is not available for IC443 as the source is located outside the survey footprint. The DRAO polarized fraction Π is computed using the total intensity value I measured from the Reich & Reich (1986) map at the same frequency. Finally, the debiasing employed to compute P can result in a final null flux density, especially when the signal-to-noise ratio for Q and U is low; in that case we quote the 95 per cent confidence level as the upper limit for the polarized flux density. The same considerations apply to the polarization fraction Π. Notice that the tables report the flux densities as they are obtained from the photometric measurements, prior to any colour correction; the CC coefficients are reported in the last column of each table. For all three regions, the corresponding SEDs in I and P are plotted in Fig. 8, while the frequency dependence of the polarization angle is shown in Fig. 9. Unlike the tables, the plots show the final colour-corrected SEDs from the last iteration of the multicomponent fit described in Section 6.1.

6 MODELLING THE SOURCE EMISSIONS

This section is devoted to the physical interpretation of the flux densities measured towards the three sources considered in this work, taking into account both the total intensity and the polarization SEDs.

6.1 Methodology

Our modelling of the source emissions considers the four continuum foreground mechanisms listed in Section 1. At low frequency, the contribution from the synchrotron emission is modelled with a power

Downloaded from https://academic.oup.com/mnras/article/519/3/3432/6984761 by guest on 18 July 2023

Table 5. Summary table for the intensity and (when available) polarized flux densities obtained for W49 at different frequencies. Values for the Stokes parameters I, Q and U are extracted from the QUIJOTE and ancillary maps degraded to a 1 deg resolution, while the polarized intensity P, the polarized fraction Π and the polarization angle γ are computed as detailed in Section 5. The last column reports the colour correction coefficients for intensity and polarization, computed following the methodology described in Section 6.1; when polarization data are not available we quote the colour correction in total intensity only.

				W49				
Survey	Freq. (GHz)	I (Jy)	Q (Jy)	U (Jy)	P (Jy)	Π per cent	γ (deg)	CC (I, P)
Haslam	0.4	208 ± 35	–	–	–	–	–	–
Berkhuijsen	0.8	167 ± 23	–	–	–	–	–	–
Reich	1.4	134 ± 16	–	–	–	–	–	–
DRAO	1.4	–	0.7 ± 2.1	4.5 ± 1.3	4.2 ± 1.7	$3.2^{+1.3}_{-1.4}$	-40.4 ± 12.9	–
Jonas	2.3	105 ± 13	–	–	–	–	–	–
Urumqi	4.8	150 ± 16	2.6 ± 7.8	3.6 ± 7.8	$\lesssim 17.0$	$\lesssim 11.2$	-26.9 ± 50.6	–
QUIJOTE	11.1	143 ± 8	1.9 ± 0.6	0.6 ± 0.5	1.9 ± 0.6	$1.3^{+0.4}_{-0.5}$	-8.4 ± 7.7	0.986, 0.974
QUIJOTE	12.9	148 ± 8	1.3 ± 0.6	0.2 ± 0.3	1.2 ± 0.4	0.8 ± 0.3	-4.5 ± 6.1	1.001, 0.998
QUIJOTE	16.8	158 ± 9	1.2 ± 0.3	0.2 ± 0.2	1.2 ± 0.3	0.7 ± 0.2	-3.8 ± 5.4	1.007, 1.019
QUIJOTE	18.8	160 ± 9	1.2 ± 0.3	0.2 ± 0.2	1.2 ± 0.3	0.8 ± 0.2	-4.7 ± 5.3	1.008, 1.012
WMAP	22.8	161 ± 6	1.0 ± 0.3	0.3 ± 0.2	1.1 ± 0.2	0.7 ± 0.1	-7.8 ± 4.8	0.973, 0.960
Planck-LFI	28.4	149 ± 6	1.0 ± 0.2	0.1 ± 0.2	1.0 ± 0.2	0.7 ± 0.1	-2.9 ± 4.1	1.006, 1.002
WMAP	33.0	144 ± 5	0.8 ± 0.3	0.1 ± 0.2	0.8 ± 0.3	0.5 ± 0.2	-1.8 ± 8.2	0.982, 0.978
WMAP	40.6	134 ± 4	0.5 ± 0.4	0.3 ± 0.3	$0.4^{+0.2}_{-0.4}$	$\lesssim 0.9$	-16.7 ± 16.1	0.994, 0.992
Planck-LFI	44.1	132 ± 5	0.4 ± 0.2	0.1 ± 0.2	0.3 ± 0.2	$0.2^{+0.1}_{-0.2}$	-7.3 ± 15.2	0.992, 0.991
WMAP	60.8	130 ± 5	0.0 ± 0.4	0.4 ± 0.6	$\lesssim 1.2$	$\lesssim 0.9$	-42.4 ± 33.8	0.977, 0.985
Planck-LFI	70.4	137 ± 6	1.0 ± 0.3	0.5 ± 0.3	1.1 ± 0.3	$0.7^{+0.3}_{-0.2}$	-14.8 ± 8.3	0.984, 0.985
WMAP	93.5	189 ± 9	1.5 ± 2.0	0.0 ± 1.6	$\lesssim 4.3$	$\lesssim 2.3$	-0.7 ± 31.3	0.993, 1.000
Planck-HFI	100.0	220 ± 11	3.4 ± 0.5	-0.1 ± 0.3	3.4 ± 0.4	1.5 ± 0.2	1.1 ± 2.4	0.965, 0.945
Planck-HFI	143.0	493 ± 24	9.6 ± 1.5	-0.2 ± 0.9	9.6 ± 1.2	1.9 ± 0.3	0.6 ± 2.7	0.984, 0.979
Planck-HFI	217.0	2021 ± 109	43.2 ± 6.5	5.7 ± 4.2	43.2 ± 5.2	2.1 ± 0.3	-3.7 ± 2.8	0.898, 0.896
Planck-HFI	353.0	9666 ± 573	190.2 ± 31.7	43.9 ± 18.6	$193.7^{+24.2}_{-24.3}$	2.0 ± 0.3	-6.5 ± 2.9	0.896, 0.900
Planck-HFI	545.0	$(3.58 \pm 0.28) \times 10^4$	–	–	–	–	–	0.887
Planck-HFI	857.0	$(1.18 \pm 0.09) \times 10^5$	–	–	–	–	–	0.961
DIRBE	1249.1	$(2.66 \pm 0.32) \times 10^5$	–	–	–	–	–	0.996
DIRBE	2141.4	$(4.14 \pm 0.50) \times 10^5$	–	–	–	–	–	1.075
DIRBE	2997.9	$(2.13 \pm 0.26) \times 10^5$	–	–	–	–	–	1.086

law:

$$S_{\rm sync}(\nu) = A_{\rm s} \left(\frac{\nu}{\nu_{\rm p}}\right)^{\alpha_{\rm s}}, \tag{2}$$

with a pivot frequency $\nu_{\rm p} = 1\,{\rm GHz}$; we fit in this case for the synchrotron amplitude $A_{\rm s}$ at 1 GHz, and for the synchrotron spectral index $\alpha_{\rm s}$. We will consider the synchrotron contribution both in intensity and polarization.

The free–free flux density as a function of frequency is given by (see for example Wilson, Rohlfs & Hüttemeister 2009):

$$S_{\rm ff}(\nu) = \frac{2k_{\rm B}\nu^2\Omega}{c^2} T_{\rm e} \left(1 - e^{-\tau_{\rm ff}(\nu)}\right), \tag{3}$$

which is the radiation transfer equation for the free–free emission, with the first fraction representing the conversion factor between brightness temperature and flux density in the Rayleigh–Jeans limit; $k_{\rm B}$ is the Boltzmann constant, c the speed of light, $T_{\rm e}$ the electron temperature and Ω the solid angle subtended by the chosen photometry aperture. All the information on the emission is encoded in the free–free opacity $\tau_{\rm ff}$, for which we adopt the parametrization provided by Draine (2011):

$$\tau_{\rm ff}(\nu) = 5.468 \times 10^{-2} \left(\frac{T_{\rm e}}{\rm K}\right)^{-1.5} \left(\frac{\nu}{\rm GHz}\right)^{-2} \times \left(\frac{\rm EM}{\rm pc\,cm^{-6}}\right) g_{\rm ff}(\nu), \tag{4}$$

where the frequency ν, the electron temperature $T_{\rm e}$ and the emission measure EM are expressed in convenient units, and $g_{\rm ff}$ is the Gaunt factor. For the latter we also choose the parametrization given in Draine (2011), namely:

$$g_{\rm ff}(\nu) = = \ln\left[\exp\left(5.960 - \frac{\sqrt{3}}{\pi}\ln\left[Z\left(\frac{\nu}{\rm GHz}\right)\left(\frac{T_{\rm e}}{10^4\,{\rm K}}\right)^{-3/2}\right]\right) + e\right], \tag{5}$$

where e is Napier's constant and we set the charge number to $Z = 1$ (hydrogen plasma). This modelling for the free–free emission is found to be more accurate than the conventional one (Wilson et al. 2009) over a broader frequency range, and was also employed in Planck Collaboration XVI (2014a). We want to fit for the value of the emission measure EM, which is defined as the squared electron density integrated along the line of sight and is generally adopted as an indicator of the strength of the free–free emission. Notice that it would not be possible to fit simultaneously for the emission measure and the electron temperature, given the strong degeneracy between the two parameters that is clear from equation (4). For the electron temperature we then adopt the values extracted from the public *Planck* COMMANDER free–free maps; more specifically, for each region we take the average of the $T_{\rm e}$ values found in the same aperture used to extract the flux density. We obtain the values 7000 K for both W49 and W51, and 6861 K for IC443.

Downloaded from https://academic.oup.com/mnras/article/519/3/3432/6984761 by guest on 18 July 2023

Table 6. Same as in Table 5, but for the W51 region.

Survey	Freq. (GHz)	I (Jy)	Q (Jy)	U (Jy)	P (Jy)	Π per cent	γ (deg)	CC (I, P)
				W51				
Haslam	0.4	684 ± 83	–	–	–	–	–	–
Berkhuijsen	0.8	653 ± 71	–	–	–	–	–	–
Reich	1.4	411 ± 43	–	–	–	–	–	–
DRAO	1.4	–	4.3 ± 2.1	-6.3 ± 1.9	$7.4^{+2.0}_{-2.1}$	$1.8^{+0.6}_{-0.5}$	27.8 ± 7.7	–
Jonas	2.3	591 ± 61	–	–	–	–	–	–
Urumqi	4.8	657 ± 66	-3.0 ± 8.4	2.7 ± 8.4	$\lesssim 17.8$	$\lesssim 2.7$	-68.9 ± 58.8	–
QUIJOTE	11.1	508 ± 25	-4.4 ± 0.8	-0.7 ± 0.7	4.4 ± 0.7	$0.8^{+0.2}_{-0.1}$	85.3 ± 4.4	0.982, 0.975
QUIJOTE	12.9	499 ± 25	-5.6 ± 0.6	-4.2 ± 0.8	6.9 ± 0.7	1.4 ± 0.2	71.5 ± 2.9	1.001, 0.998
QUIJOTE	16.8	502 ± 25	-2.6 ± 0.4	-3.4 ± 0.5	4.3 ± 0.4	0.8 ± 0.1	64.0 ± 2.8	1.008, 1.018
QUIJOTE	18.8	504 ± 25	-3.2 ± 0.5	-4.0 ± 0.4	5.1 ± 0.5	1.0 ± 0.1	64.3 ± 2.8	1.008, 1.011
WMAP	22.8	498 ± 15	-3.2 ± 0.2	-2.4 ± 0.4	4.0 ± 0.3	0.8 ± 0.1	71.3 ± 2.4	0.971, 0.963
Planck-LFI	28.4	470 ± 14	-3.4 ± 0.3	-1.8 ± 0.3	3.8 ± 0.3	0.8 ± 0.1	76.4 ± 2.5	1.006, 1.004
WMAP	33.0	466 ± 14	-3.1 ± 0.4	-1.6 ± 0.4	3.5 ± 0.4	0.7 ± 0.1	76.2 ± 3.2	0.982, 0.979
WMAP	40.6	435 ± 13	-2.9 ± 0.5	-1.4 ± 0.4	3.2 ± 0.5	0.7 ± 0.1	77.4 ± 3.8	0.995, 0.993
Planck-LFI	44.1	426 ± 13	-2.9 ± 0.2	-1.6 ± 0.3	3.3 ± 0.3	0.8 ± 0.1	75.5 ± 2.6	0.993, 0.991
WMAP	60.8	405 ± 14	-2.1 ± 0.9	-1.4 ± 0.5	2.4 ± 0.7	0.6 ± 0.2	72.5 ± 7.6	0.976, 0.972
Planck-LFI	70.4	406 ± 14	-1.4 ± 0.6	-1.2 ± 0.5	1.7 ± 0.5	0.4 ± 0.1	70.2 ± 8.1	0.985, 0.982
WMAP	93.5	481 ± 23	-1.3 ± 3.0	-1.1 ± 1.9	$\lesssim 5.4$	$\lesssim 1.1$	69.7 ± 41.1	0.988, 0.985
Planck-HFI	100.0	529 ± 21	0.4 ± 0.7	-1.9 ± 0.4	1.8 ± 0.6	0.3 ± 0.1	39.0 ± 10.8	0.976, 0.970
Planck-HFI	143.0	957 ± 43	7.3 ± 2.2	2.5 ± 1.3	7.5 ± 1.7	0.8 ± 0.2	-9.5 ± 5.4	0.986, 0.970
Planck-HFI	217.0	3545 ± 197	39.3 ± 9.2	15.1 ± 4.7	41.6 ± 6.6	1.2 ± 0.2	-10.5 ± 3.7	0.900, 0.870
Planck-HFI	353.0	$(1.63 \pm 0.10) \times 10^4$	159.5 ± 43.1	93.0 ± 19.9	182.3 ± 29.3	1.1 ± 0.2	-15.1 ± 4.3	0.898, 0.870
Planck-HFI	545.0	$(6.08 \pm 0.48) \times 10^4$	–	–	–	–	–	0.887
Planck-HFI	857.0	$(2.06 \pm 0.16) \times 10^5$	–	–	–	–	–	0.958
DIRBE	1249.1	$(4.82 \pm 0.59) \times 10^5$	–	–	–	–	–	0.982
DIRBE	2141.4	$(8.66 \pm 1.06) \times 10^5$	–	–	–	–	–	1.081
DIRBE	2997.9	$(5.60 \pm 0.68) \times 10^5$	–	–	–	–	–	1.072

Table 7. Same as in Table 5, but for the IC443 region.

Survey	Freq. (GHz)	I (Jy)	Q (Jy)	U (Jy)	P (Jy)	Π per cent	γ (deg)	CC (I, P)
				IC443				
Haslam	0.4	130 ± 14	–	–	–	–	–	–
Berkhuijsen	0.8	132 ± 13	–	–	–	–	–	–
Reich	1.4	81 ± 8	–	–	–	–	–	–
DRAO	1.4	–	0.2 ± 3.3	3.6 ± 3.5	$\lesssim 8.9$	$\lesssim 11.0$	-43.4 ± 26.4	–
Urumqi	4.8	88 ± 8	1.6 ± 1.0	-0.2 ± 1.0	$0.9^{+0.8}_{-0.9}$	$\lesssim 4.0$	3.1 ± 18.2	–
QUIJOTE	11.1	57 ± 3	1.0 ± 0.2	0.6 ± 0.1	1.1 ± 0.1	1.9 ± 0.3	-15.8 ± 3.5	0.977, 0.977
QUIJOTE	12.9	54 ± 3	0.4 ± 0.1	1.1 ± 0.1	1.2 ± 0.1	2.1 ± 0.3	-36.2 ± 3.6	1.000, 0.999
QUIJOTE	16.8	52 ± 3	0.3 ± 0.2	0.6 ± 0.1	0.7 ± 0.2	$1.3^{+0.3}_{-0.4}$	-31.2 ± 7.8	1.008, 1.017
QUIJOTE	18.8	51 ± 3	0.1 ± 0.3	0.4 ± 0.4	$\lesssim 0.9$	$\lesssim 1.8$	-40.4 ± 25.6	1.008, 1.011
WMAP	22.8	47 ± 2	0.4 ± 0.2	0.7 ± 0.1	0.8 ± 0.1	1.7 ± 0.3	-29.6 ± 4.9	0.966, 0.965
Planck-LFI	28.4	42 ± 2	0.8 ± 0.1	0.4 ± 0.1	0.9 ± 0.1	2.1 ± 0.3	-13.8 ± 3.5	1.005, 1.005
WMAP	33.0	40 ± 2	0.4 ± 0.3	0.6 ± 0.2	0.7 ± 0.2	1.7 ± 0.6	-26.0 ± 10.3	0.980, 0.981
WMAP	40.6	37 ± 2	0.3 ± 0.3	0.5 ± 0.5	$0.4^{+0.2}_{-0.4}$	$\lesssim 3.5$	-31.8 ± 15.1	0.994, 0.994
Planck-LFI	44.1	35 ± 2	0.5 ± 0.3	0.6 ± 0.3	$0.6^{+0.3}_{-0.4}$	$1.8^{+0.9}_{-1.0}$	-24.5 ± 12.5	0.992, 0.992
WMAP	60.8	33 ± 5	0.5 ± 1.4	0.8 ± 1.3	$\lesssim 3.0$	$\lesssim 9.3$	-29.1 ± 40.9	0.975, 0.973
Planck-LFI	70.4	33 ± 5	-0.1 ± 0.4	1.0 ± 0.3	1.0 ± 0.4	$2.9^{+1.2}_{-1.4}$	-47.6 ± 11.4	0.984, 0.984
WMAP	93.5	43 ± 11	0.6 ± 2.2	-0.4 ± 2.7	$\lesssim 5.0$	$\lesssim 11.6$	15.3 ± 102.5	0.989, 0.983
Planck-HFI	100.0	48 ± 11	0.3 ± 0.4	0.5 ± 0.3	0.3 ± 0.3	$\lesssim 2.8$	-28.9 ± 20.6	0.975, 0.988
Planck-HFI	143.0	80 ± 23	0.5 ± 0.6	1.0 ± 0.7	$0.9^{+0.5}_{-0.7}$	$\lesssim 3.4$	-32.0 ± 15.4	0.991, 0.987
Planck-HFI	217.0	282 ± 84	3.7 ± 3.4	2.9 ± 2.6	$2.8^{+2.3}_{-2.8}$	$\lesssim 4.2$	-19.3 ± 17.8	0.910, 0.893
Planck-HFI	353.0	1205 ± 353	15.8 ± 14.6	11.7 ± 10.0	$12.6^{+8.9}_{-12.6}$	$\lesssim 4.1$	-18.2 ± 17.2	0.907, 0.884
Planck-HFI	545.0	3934 ± 1142	–	–	–	–	–	0.900
Planck-HFI	857.0	$(1.09 \pm 0.31) \times 10^4$	–	–	–	–	–	0.970
DIRBE	1249.1	$(2.00 \pm 0.31) \times 10^4$	–	–	–	–	–	1.013
DIRBE	2141.4	$(2.54 \pm 0.40) \times 10^4$	–	–	–	–	–	1.060
DIRBE	2997.9	$(1.21 \pm 0.20) \times 10^4$	–	–	–	–	–	1.088

Downloaded from https://academic.oup.com/mnras/article/519/3/3432/6984761 by guest on 18 July 2023

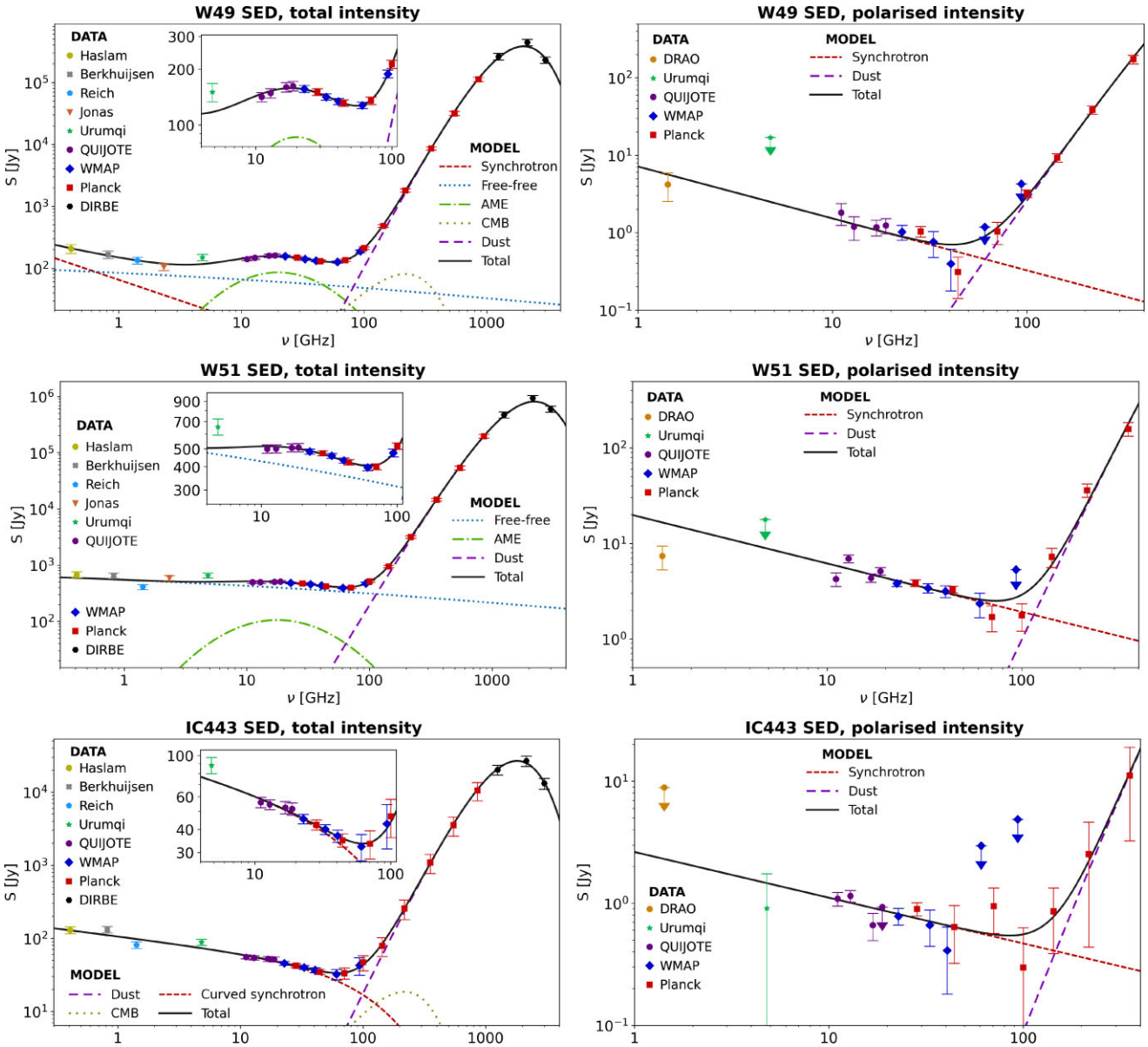

Figure 8. SEDs for W49, W51 and IC443, obtained from the combination of QUIJOTE and ancillary data, for the total intensity I (left-hand panels) and the total polarized intensity P (right-hand panels). The flux densities have been obtained via aperture photometry in a 1-deg radius aperture centred on the source, as detailed in Section 5, considering all maps smoothed at a 1 deg resolution. QUIJOTE points are the only available data for these regions covering the range between 10 and 20 GHz. Overplotted to the data points we show the best-fitting models discussed in Section 6.2; the foregrounds considered for each fit are quoted in the plot legends. In total intensity the model plotted here for W49 is the one including a synchrotron component with a fixed spectral index (third column in Table 8), the model for W51 is the one with no synchrotron component (second column in Table 9), and for IC443 we show the model with a broken power-law synchrotron spectrum (last column of Table 10). When fitting for a dust component on the polarized SEDs, the dust temperature is always fixed to the value obtained in total intensity; for W51, the DRAO point was not included in the polarization fit.

The thermal emission from ISM dust grains is clearly evident in the FIR intensity SEDs for all regions. As customary, we model this emission as a modified blackbody, where in the optically thin regime the dust blackbody spectrum $B_\nu(T_{\rm dust})$ is weighted by the dust optical depth $\tau_{\rm dust}$:

$$S_{\rm dust}(\nu) = \tau_{\rm dust}(\nu) B_\nu(T_{\rm dust})\Omega = \\ = \tau_{250}\left(\frac{\nu}{1200\,{\rm GHz}}\right)^{\beta_{\rm dust}} B_\nu(T_{\rm dust})\Omega. \quad (6)$$

In the second equality, we expressed the frequency scaling for the dust opacity as a power law around a pivot frequency of 1200 GHz (or 250 μm). In this case we fit for the dust temperature $T_{\rm dust}$, emissivity $\beta_{\rm dust}$, and optical depth τ_{250} at 250 μm.

The AME emission is modelled phenomenologically as a parabola in the log–log plane (Stevenson 2014):

$$S_{\rm AME}(\nu) = A_{\rm AME} \cdot \exp\left\{-\frac{1}{2}\left[\frac{\ln(\nu/\nu_{\rm AME})}{W_{\rm AME}}\right]^2\right\}. \quad (7)$$

In this case we fit for the peak frequency $\nu_{\rm AME}$, the peak amplitude $A_{\rm AME}$ and the width of the parabola $W_{\rm AME}$. A similar form for the AME fitting function, although with a different meaning of the parameters, was proposed by Bonaldi et al. (2007), and employed

Downloaded from https://academic.oup.com/mnras/article/519/3/3432/6984761 by guest on 18 July 2023

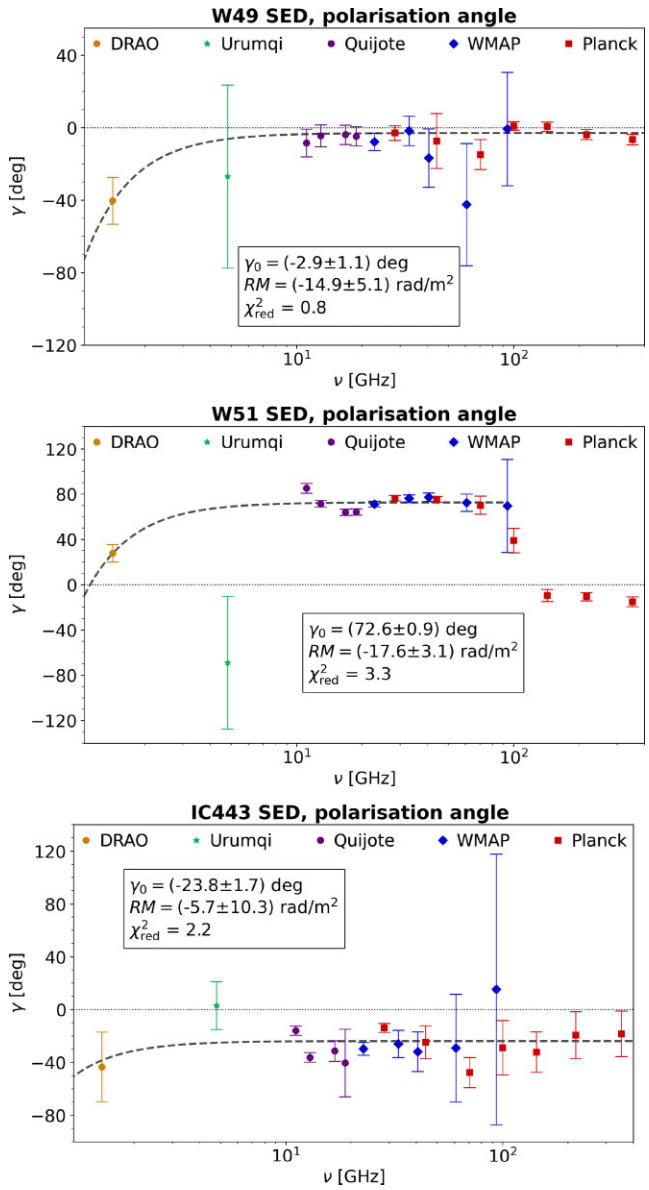

Figure 9. Polarization angle γ as a function of frequency, towards the three regions. We also overplot to the data points the best-fitting Faraday rotation model from equation (9), and report the resulting parameter estimates in each panel.

in the previous QUIJOTE publications. Such a model, however, has the drawback of coupling the peak frequency and the width of the parabola (meaning that variations in $\nu_{\rm AME}$ would alter the value of $W_{\rm AME}$). The functional form from equation (7), instead, disentangles the parameters $\nu_{\rm AME}$ and $W_{\rm AME}$, which can now be varied independently.

Finally, we fit for a CMB contribution, expressed as the differential of the flux density with respect to the temperature times the CMB temperature fluctuation $\Delta T_{\rm CMB}$:

$$S_{\rm CMB}(\nu) = \frac{h^2\nu^4}{2k_{\rm B}T_{\rm CMB}^2c^2}\sinh^{-2}\left(\frac{h\nu}{2k_{\rm B}T_{\rm CMB}}\right)\Omega\,\Delta T_{\rm CMB}, \tag{8}$$

where h is the Planck's constant and we adopt the reference CMB temperature $T_{\rm CMB} = 2.7255$ K (Fixsen 2009). In this case we fit for the value of $\Delta T_{\rm CMB}$.

The SED modelling is done with a Levenberg–Marquardt least-square fit (Markwardt 2009) between our data points and the sum of the chosen foreground models, implemented via the Interactive Data Language (IDL) MPFITFUN function.[11] As anticipated in Section 5, the model is used to compute colour correction coefficients for all frequencies above 10 GHz; these corrections are applied to the original flux densities and to their original uncertainties, and the fit is repeated, until convergence. The same procedure is adopted for both the intensity and polarization SEDs. Before choosing the final model that best reproduces the SED of each source, we explore all different foreground combinations; this iterative correction process is applied consistently in each case.

Notice that the χ^2 minimization performed in our fit assumes that all measurements are statistically independent. This is not entirely true for adjacent QUIJOTE frequencies belonging to the same horn, whose noise is correlated (see Rubiño-Martín et al. 2022, for a more complete discussion). We check for the effect this correlation can have on our source modelling in the following way. We combine the 11 and 13 GHz flux densities and errors into an effective 12 GHz measurement, using the correlation coefficients reported in Rubiño-Martín et al. (2022) when computing the effective uncertainty; the same procedure is repeated for the 17 and 19 GHz points, yielding and effective 18 GHz flux density estimate. When repeating the fit using this set of reduced QUIJOTE data, we find that the resulting best-fitting parameters are compatible within their uncertainties with the full QUIJOTE data case. We therefore conclude that the existing noise correlations between adjacent QUIJOTE frequencies are negligible as far as our source modelling is concerned.

Information on the polarized emission can also be extracted from the frequency dependence of the polarization angle shown in Fig. 9. Variations of γ with frequency can be ascribed to Faraday rotation from the neighbouring ionized medium. The effect can be modelled, as a function of wavelength, as:

$$\gamma(\lambda) = \gamma_0 + {\rm RM}\,\lambda^2, \tag{9}$$

where γ_0 is the polarization angle for $\lambda = 0$ (or $\nu \to \infty$) and RM is the rotation measure, which is proportional to the line-of-sight integral of the electron density times the parallel component of the magnetic field. We fit for γ_0 and RM over our measured γ values, and report the best-fitting estimates in each panel in Fig. 9. The resulting model for the polarization angle is overplotted as a dashed line to the data.

6.2 Application to W49, W51, and IC443

The SEDs in total intensity shown in Fig. 8 can be modelled by a suitable combination of the four foregrounds mentioned in the beginning of this section. The contribution of thermal dust emission is clear in all the regions, producing the characteristic peak at FIR frequencies. The spectrum in the lowest frequency range shows a decrease which is due to either synchrotron or free–free emission, or a combination of the two. Any possible AME contribution would emerge in the microwave range as an excess signal with respect to the combination of synchrotron and the thermal emissions. The actual detection of AME towards these regions is then subject to a clear characterization of the other foregrounds; this is particularly crucial for the low frequency points, where the free–free and synchrotron components are degenerate. For each region we will then repeat the fit by fixing the spectral index of the synchrotron power law to the

[11] https://www.l3harrisgeospatial.com/docs/mpfitfun.html.

Downloaded from https://academic.oup.com/mnras/article/519/3/3432/6984761 by guest on 18 July 2023

value estimated from the polarized intensity SED, and fit only for its amplitude. We try different combinations of the four foreground emissions and finally quote the results that provide the best modelling of the measured SED; this is assessed evaluating both the resulting χ^2 and the physical meaning of the best-fit parameter values. A summary of the fit results is reported in Tables 8, 9 and 10 for W49, W51 and IC443, respectively. The tables report the best-fit parameter values, the associated χ^2 and the corresponding reduced chi-square defined as $\chi^2_{\rm red} = \chi^2/{\rm dof}$, where the number of degree of freedom (dof) is computed as the number of fitted points minus the number of free parameters.

The polarized SEDs plotted in Fig. 8 show the joint contribution from a decaying component at low frequencies, and a raising component in the FIR range. The latter is to be ascribed to thermal dust emission, which is known to be polarized with fraction up to 20 per cent in some regions of the sky (Planck Collaboration VI 2020e); in our case the polarized flux densities suggest a low degree of polarization, at the per cent level. The decaying part of the spectrum can be due either to free–free or to synchrotron. Although the former can yield a non-null residual polarization fraction at the level $\lesssim 1$ per cent (Trujillo-Bueno et al. 2002), as commented in Section 1 it is generally assumed a non-polarized foreground. The polarized signal observed towards our regions at low frequency is then most likely to be attributed to synchrotron emission.

In principle, we could adopt the functional forms from equations (2) and (6) and fit for a combination of the two foregrounds in polarization. However, our FIR polarized flux densities only cover a portion of the rising dust spectrum, which is not effective in constraining the combination of the dust parameters. For this reason, we fix the dust temperature to the value obtained from the study of the corresponding SED in total intensity, and only fit for the dust emissivity and optical depth. Notice that we also considered a possible polarized AME contribution in our SED model, using the same functional form from equation (7). However, in all cases we found that the inclusion of a polarized AME component degrades the quality of the fit and yields non-physical values for the associated parameters. We conclude that there is no proof of any measurable AME polarized emission; as such, we decided not to include this foreground in the polarization fit. The fit results for the three regions in polarization are overplotted to the colour-corrected flux densities in the right-hand panels of Fig. 8. In the fit we also kept the points that only provide upper limits on polarization, by setting their flux density to zero and using their 1-σ uncertainty.

6.2.1 W49

For W49, we find that the SED in intensity is best modelled by a combination of all the aforementioned components with the exception of synchrotron; the resulting best-fitting parameter values are listed in Table 8. Our estimates for the free–free emission measure, the CMB temperature fluctuation and the thermal dust parameters are in agreement with those obtained in[12] Planck Collaboration XVI (2014a). At low frequencies, the contribution from the free–free emission alone provides the best fit to the SED; when including a synchrotron component, the resulting best-fitting spectral index is excessively steep ($\alpha_{\rm s} \simeq -1.3$) and its amplitude $A_{\rm s}$ is compatible with zero, so that we decided not to include a synchrotron contribution. Such a result can be understood, given that the bulk of the emission comes from the H II regions associated with W49A. The signal observed in polarization towards W49 can be ascribed to the SNR W49B or, more likely, to the diffuse Galactic synchrotron emission; in any case, its contribution in total intensity is hindered by the brighter thermal *bremmstrahlung* coming from the star-forming regions. Hence, for simplicity, we decided not to include it in our source modelling; although we know that a synchrotron component is present, its inclusion yields non-physical results for its amplitude and spectral index, while only marginally changing the parameter values for the other emissions.

[12]For the value of the optical depth we refer to the *erratum* Planck Collaboration et al. (2018).

Table 8. Results of the multi-component fits for the W49 region. The table reports the best-fit values for different parameters when fitting the total intensity I and the polarized intensity P. The table also reports the results of the fit in intensity when fixing the synchrotron spectral index to the value fitted in polarization. When fitting for P the dust temperature is always fixed to the value obtained in total intensity.

	W49		
Parameter	I	I (fixed $\alpha_{\rm s}$)	P
$A_{\rm s}$ (Jy)	–	65.3 ± 31.3	7.2 ± 2.2
$\alpha_{\rm s}$	–	-0.67	-0.67 ± 0.10
EM (cm^{-6}pc)	1315 ± 84	774 ± 283	–
$A_{\rm AME}$ (Jy)	55.0 ± 7.2	85.9 ± 17.6	–
$W_{\rm AME}$	0.6 ± 0.1	0.9 ± 0.2	–
$\nu_{\rm AME}$ (GHz)	21.0 ± 1.4	20.0 ± 1.4	–
$\Delta T_{\rm CMB}$ (μK)	98 ± 67	174 ± 88	–
$\tau_{250} \times 10^3$	1.52 ± 0.26	1.53 ± 0.27	0.03 ± 0.01
$\beta_{\rm dust}$	1.75 ± 0.09	1.75 ± 0.10	1.64 ± 0.13
$T_{\rm dust}$ (K)	20.4 ± 0.9	20.4 ± 0.9	20.4
χ^2	12.3	8.9	16.8
$\chi^2_{\rm red}$	0.69	0.52	1.20

The situation is different when analysing the polarized SED, which clearly shows a decreasing spectrum at low frequencies that can be ascribed to synchrotron; we then fit the spectrum with a combination of synchrotron and thermal dust, fixing $T_{\rm dust}$ to the value obtained in total intensity. The resulting spectral index is $\alpha_{\rm s} = -0.67 \pm 0.10$, which is consistent with the expected range for the synchrotron emission. It is then possible to try and fit for a synchrotron component in total intensity, fixing the spectral index to the value obtained in polarization and only leaving the amplitude $A_{\rm s}$ as a free parameter. This time the synchrotron amplitude is detected at $2\,\sigma$, while the best-fit values for the free–free emission measure and the CMB temperature fluctuation have respectively a worse and better agreement with Planck Collaboration XVI (2014a); this can be expected as this reference does not include a synchrotron component in the source modelling, so that their free–free result accounts for the whole amplitude of the emission at low frequencies.

Still, the joint contribution of free–free, CMB and thermal dust is not enough to account for the microwave flux densities in total intensity, with QUIJOTE points clearly suggesting a downturn of the AME excess in this frequency range. We found that the inclusion of our AME functional form yields the best modelling with $\chi^2_{\rm red} = 0.69$ without synchrotron and $\chi^2_{\rm red} = 0.52$ when fixing $\alpha_{\rm s}$ (by comparison, a fit without AME would result in $\chi^2_{\rm red} = 3.60$ and $\chi^2_{\rm red} = 3.78$, respectively, with a flip in sign for the CMB temperature fluctuation). In the end, we can choose the modelling that includes the synchrotron with fixed spectral index as our reference model for W49, as it provides the best $\chi^2_{\rm red}$ value and yields physically reasonable values for all resulting parameters. The AME peak frequency is $\nu_{\rm AME} = 20.0 \pm 1.4$ GHz, where it is detected with a significance

Downloaded from https://academic.oup.com/mnras/article/519/3/3432/6984761 by guest on 18 July 2023

Table 9. Same as in Table 8, but for the W51 region.

	W51		
Parameter	I	I (fixed α_s)	P
A_s (Jy)	–	359.0 ± 140.3	19.8 ± 4.6
α_s	–	-0.51	-0.51 ± 0.07
EM (cm^{-6}pc)	2828 ± 178	428 ± 1071	–
A_{AME} (Jy)	105.6 ± 26.3	359.3 ± 121.7	–
W_{AME}	0.9 ± 0.3	1.7 ± 0.4	–
ν_{AME} (GHz)	17.7 ± 3.6	15.8 ± 3.0	–
ΔT_{CMB} (μK)	-51 ± 105	94 ± 181	–
$\tau_{250} \times 10^3$	1.08 ± 0.20	1.10 ± 0.21	0.03 ± 0.02
β_{dust}	1.65 ± 0.10	1.66 ± 0.11	2.35 ± 0.33
T_{dust} (K)	23.1 ± 1.2	22.9 ± 1.3	23.1
χ^2	22.2	19.2	29.2
χ^2_{red}	1.23	1.13	2.25

of $\sim 4.7\sigma$ and accounts for $\sim$ 55 per cent of the observed intensity emission towards W49.

W49 does not appear in QUIJOTE maps as a strongly polarized source. In Fig. 2 it is visible in Q as a local increase in the intensity of the polarized background, while there are only hints of positive U towards the source. The flux densities quoted in Table 5 confirm this picture with most of the signal coming from positive Q. Since this polarized state is typical of the diffuse Galactic plane emission, the polarization observed towards W49 may be produced by local intensification of the Galactic foreground, rather than by synchrotron emission proceeding specifically from the SNR W49B. The DRAO maps in Fig. 5 show a different configuration, in which the positive Q towards the centre of the region is smeared, while U shows a clear positive signal; this can be a result of Faraday rotation of the polarized direction showing up at the 21 cm wavelength. This observation is corroborated by the fact that the polarized intensity spectrum in Fig. 8 flattens at the lowest frequencies, suggesting a loss of polarized flux density (Faraday depolarization). The Q and U flux densities in Table 5 show that this effect already begins to be important at the Urumqi 5 GHz frequency, although their high uncertainties only provide an upper limit for P, as shown in the SED plot. A more direct representation of this effect is provided by the spectral distribution of the polarization angle in Fig. 9. While at $\nu \gtrsim$ 10 GHz the angle is constantly close to zero, which means a mainly positive Q state, the DRAO and Urumqi points show a deviation that can be fitted by our Faraday rotation model with a rotation measure $RM = (-14.9 \pm 5.1)\,\mathrm{rad\,m^{-2}}$. We stress that, although we measure a Faraday rotation effect, the associated synchrotron emission likely does not proceed from the SNR W49B, but rather from the diffuse Galactic polarized emission; as a further proof of this, we notice that the peak of the positive U emission in the DRAO map is shifted with respect to the position of W49. None the less, as this polarized signal is captured by our aperture, it is worth showing the associated modelling in P and γ as part of our study of QUIJOTE data towards this region.

6.2.2 W51

For W51 the situation is very similar to W49: the local massive molecular clouds and associated H II regions are the main source of radio emission at low frequencies, where they mask the non-thermal emission from the SNR W51C. The SED is best fitted by a combination of free–free, AME, CMB and thermal dust, with the estimates on the parameters reported in Table 9; the CMB in this case shows a negative contribution, which however is compatible with zero. Our dust parameters are in reasonably good agreement with the ones reported in Demetroullas et al. (2015), considering that their fit includes a synchrotron component and does not include AME or CMB. In our fit, the inclusion of AME determines a considerably better agreement between the model and the data points, improving the χ^2_{red} value from 2.06 to 1.23. The inclusion of a synchrotron component, instead, would make the free–free emission measure compatible with zero and yield non-physical values for the AME parameters; when keeping the synchrotron and removing the AME component we find again a free–free amplitude compatible with zero and a very flat synchrotron spectrum ($\alpha_s \simeq -0.1$). We therefore decided not to include the synchrotron component in our intensity fit.

However, unlike W49, W51 clearly stands out against the Galactic plane as a bright polarized source, with both negative Q and U. Among the three regions considered in this work, it is the one that provides the highest polarized flux densities; still, this increase in the polarized flux density is associated with an increase in the total intensity towards the source, so that the resulting polarization fractions in Table 6 are at the same level as for the other regions. Also, for W51 the effect of Faraday depolarization appears even stronger than in the case of W49: this can be seen already from the Urumqi and DRAO maps in Fig. 5. The screening effect is likely due to intervening ionized gas along the line of sight towards W51C, possibly associated with the H II regions from the neighbouring W51A. As reported in Table 6, at the Urumqi frequency the U flux density is compatible with zero, while the polarized SED in Fig. 8 shows that the DRAO point flux density is at the same level as the lowest QUIJOTE frequencies. The spectral distribution of the polarization angle shown in Fig. 9 once again confirms this picture, with a rather constant angle at microwave frequencies and a sharp decrease at $\nu \lesssim 10$ GHz. The fit of our Faraday rotation model yields $RM = (-17.6 \pm 3.1)\,\mathrm{rad\,m^{-2}}$, which is higher in modulus than the estimate obtained for W49, confirming the effect is more relevant. Note that in this case we did not include the *Planck*-HFI points in the fit, as in the plot they show a break with the microwave trend; this is probably due to polarized dust contribution, either from the diffuse Galactic background or associated with the H II regions in W51. The effect is also quite evident from the bottom row panels in Fig. 5.

Once again, the polarized SED is best fitted by a combination of a synchrotron and a thermal dust component alone. Including all our available points we obtain the values $\alpha_s = -0.37 \pm 0.05$ and $S^{1\,\mathrm{GHz}}_{sync} = 12.7 \pm 2.0$ with $\chi^2_{red} = 2.61$. Demetroullas et al. (2015) obtained the estimate $\alpha_s = -0.58 \pm 0.06$ when using CBI 31 GHz and Effelsberg 2.7 GHz data. Our flatter spectrum can be a result of Faraday depolarization at the lowest frequencies, as explained. In fact, if we remove the DRAO point from the fit and only keep frequency points from 4.8 GHz upwards (the Urumqi point only providing an upper limit), we obtain the values reported in Table 9, with the compatible estimate $\alpha_s = -0.51 \pm 0.07$. We conclude that the Faraday depolarization severely affects the DRAO point, in such a way that its inclusion in the fit would result in a biased estimation of the synchrotron spectral index. Hence, we keep the fit results obtained removing the DRAO point as our fiducial estimates.

Going back to the intensity SED, we still tried to include a synchrotron component by fixing its spectral index to the value $\alpha_s = -0.51$ fitted in polarization. Although the goodness of fit is maintained ($\chi^2_{red} = 1.13$) this modification in the modelling significantly alters the values of the emission measure (which is now compatible with zero), the CMB (again compatible with zero but positive) and the AME parameters, the latter showing an unphysically

Downloaded from https://academic.oup.com/mnras/article/519/3/3432/6984761 by guest on 18 July 2023

Table 10. Same as in Table 8, but for the IC443 region. In this case, the additional last column reports the results of the fit which adopts a broken power-law synchrotron model, and which results in the best modelling for IC433 intensity SED.

Parameter	IC443 I	I (fixed α_s)	P	I (curv. s.)
A_s (Jy)	96.5 ± 10.6	71.9 ± 10.9	2.6 ± 1.0	106.7 ± 5.8
α_s	-0.29 ± 0.03	-0.37	-0.37 ± 0.13	-0.21 ± 0.04
$\nu_{0,s}$ (GHz)	–	–	–	114 ± 73
EM (cm^{-6}pc)	69 ± 60	235 ± 39	–	–
ΔT_{CMB} (μK)	-58 ± 37	-65 ± 35	–	29 ± 54
$\tau_{250} \times 10^3$	0.09 ± 0.03	0.09 ± 0.03	0.002 ± 0.006	0.11 ± 0.04
β_{dust}	1.31 ± 0.25	1.28 ± 0.23	2.12 ± 1.49	1.51 ± 0.29
T_{dust} (K)	20.6 ± 2.0	20.7 ± 1.9	20.0	19.4 ± 1.9
χ^2	13.1	13.8	12.7	11.0
χ^2_{red}	0.73	0.72	0.90	0.61

large value for W_{AME}, and a very low value for the peak frequency. We also tried and fixed the synchrotron amplitude too, by assuming a polarization fraction of 20 per cent; from the polarization best-fitting modelling, this results in $A_s = 99$ Jy. When fixing both the synchrotron amplitude and spectral index, compared to the case of no synchrotron, we obtain compatible best-fit parameters for the thermal dust, a slightly larger value for the emission measure EM $= (2246 \pm 250)$ pc cm^{-6}, a sign-flipped CMB contribution (still compatible with zero) $\Delta T_{CMB} = (6 \pm 121)$ μK and AME parameters equal to $A_{AME} = (164 \pm 36)$ Jy, $W_{AME} = 1.2 \pm 0.4$ and $\nu_{AME} = (16.8 \pm 3.4)$ GHz, with $\chi^2_{red} = 1.15$. Although the AME width is still rather large, this example shows that the observed SED in intensity is, in fact, compatible with the inclusion of a synchrotron component at reasonable levels; however, we do not adopt this fit as our fiducial model for W51 due to the rather arbitrary value we assigned to the polarization fraction. In conclusion, the intensity SED suggests that although a synchrotron component is present in the source emission, the observed low-frequency data are best modelled by a free–free component alone, which is by far the dominant foreground emission mechanism in this frequency range. The inclusion of the AME component, on the contrary, always improves the quality of this fit, changing the χ^2_{red} from 2.17 to 1.13 (from 3.05 to 1.15 when the synchrotron amplitude is also fixed). For all these considerations, we fix the combination of free–free, AME, CMB and thermal dust, with no synchrotron, as the best model for W51 in total intensity. Towards this region AME is detected at the peak frequency $\nu_{AME} = (17.7 \pm 3.6)$ GHz with a significance of $\sim 4.0\,\sigma$, contributing to the observed intensity emission with a ~ 21 per cent in flux density. Its relative significance, then, is lower compared to W49.

6.2.3 IC443

In total intensity IC443 shows a different combination of emission mechanisms compared to the other two sources. In this case, we find that the best-fitting model consists of synchrotron (with spectral index $\alpha_s = -0.29 \pm 0.03$), free–free, CMB and thermal dust, with the parameters reported in the second column of Table 10 and a final $\chi^2_{red} = 0.73$. Any combination that does not include a synchrotron component would result in values of $\chi^2_{red} > 2$, non-physical values for most parameters and an overall bad agreement between the model and the points at low frequency. This proves that the bulk of the IC443 emission is non-thermal and proceeds from the local SNR. On the contrary, a model without a free–free component could be valid as well, yielding $\chi^2_{red} = 0.69$ and values for the other parameters compatible with those reported in the second column of Table 10. Thermal *bremmstrahlung* radiation from IC443 was initially claimed in Onić et al. (2012), although discarded by subsequent work; it is clear that free–free is a subdominant component in this region, but its presence cannot be discarded a priori. Since it is detected in our fit with reasonable values for the other parameters, it is worth including it in the source modelling. On the contrary, the inclusion of AME as an additional component would yield $\chi^2_{red} = 0.80$, with quite low values for the AME amplitude ($A_{AME} = 4.4 \pm 3.8$ Jy), width ($W_{AME} = 0.21 \pm 0.19$) and peak frequency ($\nu_{AME} = 16.3 \pm 2.7$); similar considerations hold when the CMB contribution is removed from the fit. We conclude that the measured SED in IC443 does not provide any compelling evidence for the presence of AME towards the region. We stress that dust emission towards IC443 is well-reconstructed, but its amplitude is at least one order of magnitude lower compared to W49 and W51. This suggests a limited presence of dust in the region; as AME is generally observed in association with dust, it is not likely to be observed towards IC443.

IC443 is detected in polarization across our microwave frequencies as a positive Q and U source. The low dust amplitude in total intensity also results in very low flux densities in polarization; even at lower frequencies, the flux densities in Q and U are often consistent with zero. In this case the debiasing employed to compute P flux densities is important to prevent overestimating the polarized intensity. Still, although the microwave polarized flux densities are generally below 1 Jy, in this case the position of the source outside the Galactic plane allows the detection of its polarized emission with less confusion with the background. Most likely, this polarized signal is synchrotron emission from the SNR, and it is reasonable to fit for the corresponding power law on the polarized SED. At 1.4 GHz the source still yields a positive U flux density, and a value of Q consistent with zero; the DRAO maps in Fig. 6 show hints of positive polarization signal towards the centre of the aperture, although being in general subdominant with respect to other background structures. At 5 GHz the source yields a strong positive Q flux density, and a change of sign in U. These considerations may indicate that the two lowest frequency points are once again affected by Faraday rotation, although their error bars are too large to firmly establish it. In fact, looking at the SEDs plot in Fig. 8, there seems not to be a net flux density loss below 10 GHz, and the spectrum decays as expected for a synchrotron emission. As a further confirmation, we can see from Fig. 9 that in this case the variation of the polarization angle at low frequency is very mild, and as a result our Faraday rotation fit yields a value of $RM = (-5.7 \pm 10.3)$ rad m^{-2} for the rotation measure, which is compatible with zero and considerably lower in modulus than the one measured for W49 or W51. We thus conclude that, although we observe hints of Faraday rotation towards IC443, the effect is negligible as far as our analysis is concerned. We therefore proceed with a fit for the polarized SED using all available points, and modelling again the emission as a combination of synchrotron and dust; the resulting parameters are reported in the fourth column of Table 10, with a synchrotron spectral index of $\alpha = -0.37 \pm 0.13$ and $\chi^2_{red} = 0.90$.

Going back to the SED in total intensity, when fixing the synchrotron spectral index to the value obtained in polarization, we find the best-fit is obtained with the same model adopted when the synchrotron spectral index was left free, i.e. a combination of synchrotron, free–free, CMB and thermal dust. Compared to the case of free spectral index, the synchrotron amplitude decreases while the measurement of the free–free emission measure becomes

Downloaded from https://academic.oup.com/mnras/article/519/3/3432/6984761 by guest on 18 July 2023

more significant; the parameter values associated with CMB and thermal dust, instead, are only marginally affected (third column of Table 10). Once again, the inclusion of AME would yield non-physical values for the associated parameters, especially for its peak frequency ($\nu_{\rm AME} \simeq 6$ GHz). The fact that the free–free amplitude is higher in this case can be the result of a steepening of the synchrotron spectrum at frequencies above a few GHz. In that case, because the synchrotron is fitted in polarization starting from ~ 5 GHz (the DRAO point really only provides an upper limit), we would expect the value of $\alpha_{\rm s}$ to be larger in modulus compared to the result fitted in total intensity. When forcing such a steep spectrum in the intensity SED, the fit better accommodates the lowest frequency points by lowering the synchrotron amplitude and including a flatter spectral contribution as is the one from the free–free emission. So, our detection of thermal emission in IC443 may simply be a result of an inaccurate modelling of the synchrotron spectrum across the frequency range we explore.

In order to better test this hypotesis, we also try and fit for a curved synchrotron model, which differs from the parametrization in equation (2) for the inclusion of a cut-off frequency $\nu_{0,\,\rm s}$:

$$S_{\rm sync}^{\rm curv}(\nu) = A_{\rm s}\left(\frac{\nu}{\nu_{\rm p}}\right)^{\alpha_{\rm s}} \exp\left(-\frac{\nu}{\nu_{0,\rm s}}\right). \tag{10}$$

With this model, we find that the best fit to the IC443 intensity spectrum is provided by a combination of synchrotron, CMB and thermal dust, with the best value of $\chi^2_{\rm red} = 0.61$ obtained for this region and a spectral index which is lower in modulus than the one obtained for a simple power-law synchrotron model (last column of Table 10). In this case the CMB component flips sign compared to the case of the simpler synchrotron model, although its amplitude is compatible with zero, confirming that it is a subdominant component in the SED. The inclusion of AME generally yields unphysical values for its parameters, and the inclusion of free–free results in too low a value for the synchrotron cut-off frequency (around 60 GHz). We then decided to fit IC443 as a combination of curved synchrotron, CMB and thermal dust; this is the model that is overplotted to the data points in Fig. 8, and the resulting parameters are quoted in the fifth column of Table 10.

Previous works already tackled the modelling of IC443 spectrum from radio to FIR frequencies. As already mentioned, Onić et al. (2012) claimed the detection of free–free towards the region, accounting up to 57 per cent of the observed emission at 1 GHz. Our model with a free spectral index results in a free–free amplitude of ~ 10 Jy, or ~ 10 per cent of the total, while the fixed spectral index model yields ~ 36 Jy, or ~ 33 per cent of the total; both these estimates are in agreement with the quoted result. We already stressed, however, how our finding could be simply the result of forcing too steep a synchrotron spectrum. In Planck Collaboration XIII (2016c) the existence of a thermal component was ruled out, and IC443 was modelled as a simple combination of synchrotron and thermal dust; for the latter, they quote $\beta_{\rm dust} = 1.5$, in agreement with our finding, and $T_{\rm dust} = 16$ K, which is $\sim 2\sigma$ lower than our estimate (although the reference does not quote error bars, which makes an acutal comparison unreliable). As for the synchrotron, they favour $\alpha_{\rm s} = -0.36$, compatible with our estimate in polarization, although they mention that for frequencies above 40 GHz the spectrum shows a steepening to $\alpha_{\rm s} = -1.5$. This observation corroborates our use of a curved synchrotron model. In Onić et al. (2017) the IC443 SED from 400 MHz to 143 GHz was fitted using a combination of synchrotron, thermal dust and AME (not favouring any free–free contribution). Their work also stressed the presence of a break in the synchrotron power law visible above ~ 5 GHz, and they also considered a curved synchrotron model as in our equation (10). Different implementations pointed towards a cut-off frequency in the range 112 GHz $< \nu_{0,\rm s} <$ 152 GHz and spectral index in the range $-0.39 < \alpha_{\rm s} < -0.35$; their estimates for the dust temperature are in agreement with *Planck* results, while their emissivity results are slightly higher, in the range $1.97 < \beta_{\rm dust} < 2.345$. Most importantly, they detected an excess of emission at 30 GHz which they interpreted as AME. A very similar analysis was conducted in Loru et al. (2019), measuring a curved synchrotron with $\alpha_{\rm s} = -0.38$ and $\nu_{0,\rm s} = (148 \pm 23)$ GHz, and claiming a detection of AME peaking at $\nu_{0,\rm AME} = (28 \pm 3)$ GHz. The synchrotron cut-off frequency obtained in our analysis is consistent with these results.

Although these previous works would agree in establishing the presence of AME towards IC443, there are some issues that should be pointed out. First of all, their analyses rely on the combination of flux density estimates coming from previous results in the literature, obtained using different types of radio observations, different angular resolutions and different analysis techniques. Although Onić et al. (2017) recognized the inherent risks of such an approach, which makes their study somehow qualitative, they still firmly established the need for an extra emission at microwave frequencies to account for the observed excess. Besides, both Onić et al. (2017) and Loru et al. (2019) adopted the microwave flux densities from Planck Collaboration XIII (2016c). Those flux densities were measured with aperture photometry, adopting a variable size of the aperture as a function of the considered frequency. The analysis in Planck Collaboration XIII (2016c) introduced a correction factor, equal to 1.4 for IC443, to account for the loss of flux density that is not captured inside their aperture due to the beam convolution. The authors did not applied this correction to well-resolved sources, defined as those with diameter 50 per cent larger than the beam FWHM. As the *Planck* beam FWHM decreases with increasing frequency, this criterion implies that for IC443 the correction is applied at 30 and 44 GHz, but not from 70 GHz onwards. Their analysis adapted the size of the aperture at each frequency, in such a way that the same fraction of flux density should be retained inside the aperture; hence, these correction factors should be applied to all their frequency points, and not only to 30 and 44 GHz. This approach produces an artificial dip of the SED at 70 GHz, which the authors interpreted as the downturn of AME. We can also argue that this strategy for the flux density extraction is not appropriate in cases of significant background fluctuations, as it is the case for IC443; in fact, none of those works adopted any masking around IC443, so that the aperture photometry estimation of the flux density emission and/or the background level can be easily biased by the contribution from the neighbouring sources Sh2-249 and Sh2-252. The analysis we have presented in this paper, however, not only took care of the mask, but also measured the flux densities adopting a common angular resolution and a consistent methodology (with fixed apertures and background annuli) that is applied throughout the considered frequency range. In conclusion, we do believe that the available data set points towards an absence of AME emission towards IC443; at the very least, we can affirm that if an AME component is present, it is dominated by the uncertainties in our flux density measurements, and is certainly much fainter than the emission detected towards W49 and W51. Although we still observe a dip in the IC443 spectrum around 70 GHz, it can be more reasonably fitted with a curved synchrotron component, and is not sufficiently compelling to justify the inclusion of AME at ~ 30 GHz.

Downloaded from https://academic.oup.com/mnras/article/519/3/3432/6984761 by guest on 18 July 2023

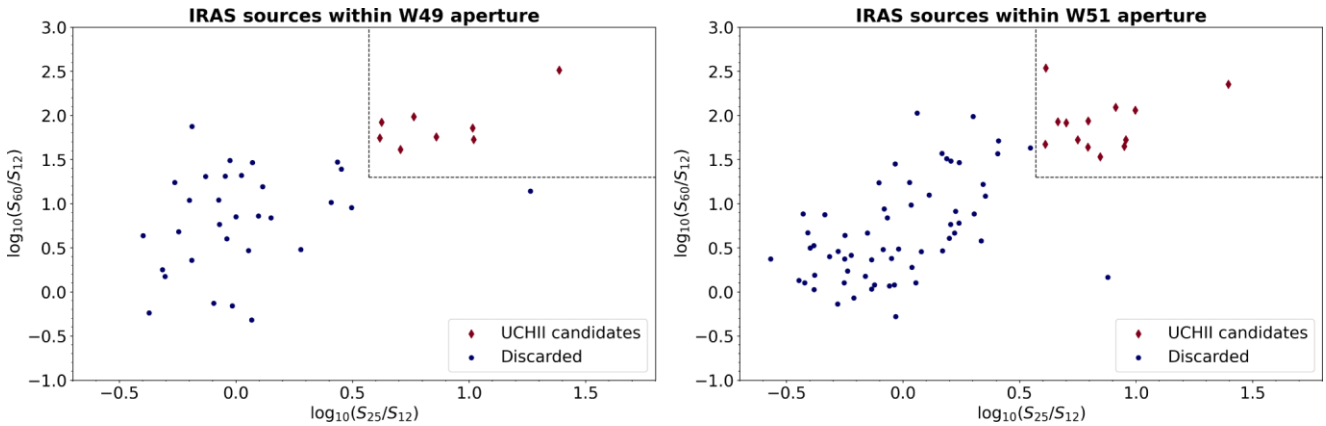

Figure 10. Extraction of candidate UCH II regions using *IRAS* data for both W49 (left-hand panel) and W51 (right-hand panel). Points represent *IRAS* Galactic IR sources entering the aperture employed for the photometric study of each region, displayed in a colour–colour plot based on *IRAS* measured flux densities. UCH II regions are expected to yield ratios $\log_{10}(S_{60}/S_{12}) \gtrsim 1.30$ and $\log_{10}(S_{25}/S_{12}) \gtrsim 0.57$; the group of sources satisfying these conditions is shown with red diamonds, with the dashed lines marking the flux density boundaries. In this way we select 8 sources for W49 and 13 sources for W51, and use them to estimate the contamination from UCH II to our AME detections. See Section 6.3.1 for details.

6.3 Further considerations on AME

We conclude our analysis by commenting some further aspects related to the detection of AME in W49 and W51. First of all, we have to stress that, because we are working with maps smoothed at a 1-deg angular resolution and we use apertures of typical radius of ~ 1 deg, the measured flux densities may have a significant contribution from the region neighbouring each source. Therefore, although we detect AME towards W49 and W51, it is hard to assess whether the measured signal proceeds entirely from the sources or has an important contribution from the diffuse Galactic emission in their surroundings. Although in the rest of this section we will still discuss about AME emission from W49 and W51, it is important to acknowledge this possibility. Further discussion about this matter can be found in Appendix A.

6.3.1 Contribution from ultracompact H II regions

UCH II regions are produced by recently formed massive stars which are still embedded in their molecular clouds; those with EM $\gtrsim 10^7$ cm^{-6}pc can have a significant optically thick free–free emission at frequencies up to 10 GHz or higher. This emission can produce an excess in the measured flux density at QUIJOTE frequencies, thus mimicking the effect of AME on the SEDs of W49 and W51. The goal of this section is to assess to what extent the contribution from UCH II can affect the significance of our AME detection.

At first we follow the procedure described in Planck Collaboration XVI (2014a) and also adopted by Poidevin et al. (2022), to which we redirect for a more detailed explanation and further references. This method is based on the extraction of candidate UCH II sources entering our chosen apertures and on the estimation of their total flux density at AME frequencies. For this we employ data from the *IRAS* Point Source Catalogue,[13] which provides flux density measurements for point sources at 12, 25, 60 and 100 μm. For both W49 and W51 we query the catalogue to extract the IR sources contained in the aperture employed for our photometric flux density measurements; in addition, we discard sources which are extra-Galactic or upper limits in either 25 μm or 60 μm. We then place the retrieved IR sources on a $\log_{10}(S_{25}/S_{12})$–$\log_{10}(S_{60}/S_{12})$ plane as shown in Fig. 10, where S_x denotes the *IRAS* measured flux density at wavelength x. UCH II sources are expected to have $\log_{10}(S_{60}/S_{12}) \gtrsim 1.30$ and $\log_{10}(S_{25}/S_{12}) \gtrsim 0.57$; as marked in Fig. 10, this leaves 8 IR sources in W49 and 13 sources in W51. *IRAS* data allow to evaluate the associated total flux density at 100 μm. For an UCH II region, the ratio between this flux density and the flux density at 15 GHz is found to lie in the range 1000–400 000, which allows us to place both an upper and a lower limit to the expected UCH II contamination at QUIJOTE frequencies. The results are reported in Table 11, where they are compared with the residual AME amplitudes at the same frequency. We see that in the worst case scenario the contribution from UCH II sources can account for ~ 55 per cent of the AME flux density towards W49, and for ~ 32 per cent of the AME flux density towards W51. We stress that this not only is an upper limit, but according to Planck Collaboration XVI (2014a) it is also likely overestimated by a factor of a few. The corresponding lower limit estimate is completely negligible compared to the measured AME flux density, which confirms our detection of AME cannot be ruled out on the basis of this simple extrapolation.

Table 11. Results for the contribution from UCH II regions in W49 and W51. We report the AME residual amplitude at 15 GHz, $S^{\rm AME}_{\rm 15GHz}$, the measured UCH II total flux at 100 μm from IRAS data, $S^{\rm IRAS}_{\rm 100\mu m}$, and its corresponding upper and lower limit extrapolations at 15 GHz, $S^{\rm uplim}_{\rm 15GHz}$ and $S^{\rm lowlim}_{\rm 15GHz}$. The last column reports the total UCH II flux measured with CORNISH data at 5 GHz.

Source	$S^{\rm AME}_{\rm 15GHz}$ (Jy)	$S^{\rm IRAS}_{\rm 100\mu m}$ (Jy)	$S^{\rm uplim}_{\rm 15GHz}$ (Jy)	$S^{\rm lowlim}_{\rm 15GHz}$ (Jy)	$S^{\rm CORNISH}_{\rm 5GHz}$ (Jy)
W49	81.4	45098	45.1	0.1	8.5
W51	103.9	33368	33.4	0.1	5.3

In order to get an independent estimate of the possible contamination from UCH II regions, we consider data from the CORNISH[14] continuum survey of the Galactic plane at 5 GHz with a 1.5 arcsec resolution (Purcell et al. 2013). CORNISH legacy data include a

[13] https://heasarc.gsfc.nasa.gov/W3Browse/iras/iraspsc.html.

[14] Co-Ordinated Radio 'N' Infrared Survey for High-mass star formation, https://cornish.leeds.ac.uk/public/index.php.

Downloaded from https://academic.oup.com/mnras/article/519/3/3432/6984761 by guest on 18 July 2023

catalogue of identified UCH II regions, which we query to select the ones entering our apertures. We find 24 sources within the W49 aperture and 8 sources within the W51 aperture, contributing with the 5 GHz flux densities quoted in Table 11. Now, there is no standard way to extrapolate these flux densities to the peak frequency of our AME detection. None the less, we can refer to the SEDs plotted in Kurtz, Churchwell & Wood (1994) for several different UCH II regions, which were built using VLA integrated flux density measurements at 8.3 and 15 GHz in combination with *IRAS* flux densities and other ancillary data. The plots do not show any appreciable variation of the spectrum for frequencies $\lesssim 100$ GHz. Hence, to a first approximation we can extrapolate our UCH II flux density measurements at 5 GHz to 15 GHz for a comparison with the corresponding AME residuals. We find that the contribution from UCH II amounts to ~ 10 per cent of the AME amplitude in W49 and to ~ 5 per cent in W51. We conclude that, although a non-negligible contribution from UCH II is entering our measured flux densities, it is not enough to account for the local SED excess amplitude and rule out the presence of AME. Novel, tailored observations to these regions are required to better constrain the UCH II contribution.

6.3.2 Constraints on AME polarization

One of the driving goals of this analysis was the search for a possible polarized AME emission, which has not been detected to date and could shed light on the mechanism responsible for this foreground (Section 1). We have already commented that for both W49 and W51 the polarized SED is suitably modelled by a combination of synchrotron emission and dust emission alone. Although AME is not directly detected in our polarization fits, we can proceed in a way similar to what was done in Génova-Santos et al. (2017) and Poidevin et al. (2019) to quote upper limits for the AME polarization fraction.

We proceed as follows. We consider the frequency points where AME is most significant and less affected by other foregrounds, i.e. those in the frequency range from 17 to 61 GHz. In this frequency range we generate a set of 1000 AME residual SEDs in intensity, computed using equation (7) and adopting random AME parameters; the latter are sampled from a Gaussian distribution centred on the best-fitting estimates from Tables 8 and 9, and scattered according to their uncertainties. The dispersion of these realizations at the chosen frequency points allows us to evaluate the uncertainty for the local AME intensity $I_{\rm AME}$. The resulting flux densities are quoted in Table 12, together with the polarized P flux densities at the same frequencies.[15] We then compute the associated polarization fractions as $P/I_{\rm AME}$, which are reported in the fourth column of Table 12 in per cent units.

Clearly, we know that at these frequencies an important polarized contribution comes from both the synchrotron and the dust emission. These fractions should therefore be interpreted as upper limits on the AME polarization fraction. In fact, while the AME intensity peaks around 20 GHz, the polarized flux densities steadily decrease over the considered frequency range, and are most likely associated with synchrotron. For this reason, in the last column of Table 12 we report explicitly the upper limits on the AME polarization fraction $\Pi_{\rm AME}$, which are computed as the 95 per cent confidence level upper boundaries of the $P/I_{\rm AME}$ values. We can quote the tightest constraints

[15]The P values in Table 12 have been colour-corrected using the CC coefficients reported in the last column of Tables 5 and 6; hence, they are slightly different from the polarized flux densities already quoted in the photometric analysis section.

Table 12. AME polarization constraints from 16 to 61 GHz. For each frequency point we report the local residual AME amplitude $I_{\rm AME}$, the colour-corrected polarized flux P, the resulting polarization fraction $P/I_{\rm AME}$ and the associated upper limit for the AME polarization fraction $\Pi_{\rm AME}$, computed as the 95 per cent confidence level upper boundary on the fraction $P/I_{\rm AME}$. When no uncertainty on $P/I_{\rm AME}$ is quoted it means the debiased P flux is null and the reported upper limit is already the top boundary of the 95 per cent confidence level.

		W49		
Freq. (GHz)	$I_{\rm AME}$ (Jy)	P (Jy)	$P/I_{\rm AME}$ (per cent)	$\Pi_{\rm AME}$ (per cent)
16.8	84.2 ± 17.3	1.2 ± 0.3	1.4 ± 0.4	$\lesssim 2.3$
18.8	85.7 ± 17.5	1.2 ± 0.3	1.5 ± 0.4	$\lesssim 2.3$
22.8	84.9 ± 17.5	1.0 ± 0.2	1.2 ± 0.4	$\lesssim 1.9$
28.4	79.2 ± 17.2	1.0 ± 0.2	1.3 ± 0.4	$\lesssim 2.0$
33.0	72.8 ± 16.9	0.8 ± 0.3	1.0 ± 0.5	$\lesssim 2.0$
40.6	61.7 ± 16.6	$0.4^{+0.2}_{-0.4}$	$0.6^{+0.4}_{-0.7}$	$\lesssim 1.4$
44.1	56.8 ± 16.5	0.3 ± 0.2	$0.6^{+0.3}_{-0.4}$	$\lesssim 1.2$
60.8	38.0 ± 15.0	$\lesssim 1.2$	$\lesssim 3.1$	$\lesssim 3.1$
		W51		
Freq. (GHz)	$I_{\rm AME}$ (Jy)	P (Jy)	$P/I_{\rm AME}$ (per cent)	$\Pi_{\rm AME}$ (per cent)
16.8	105.5 ± 27.5	4.4 ± 0.4	4.1 ± 1.2	$\lesssim 6.4$
18.8	105.4 ± 28.0	5.1 ± 0.5	4.9 ± 1.4	$\lesssim 7.6$
22.8	101.7 ± 29.9	3.8 ± 0.3	3.8 ± 1.1	$\lesssim 6.0$
28.4	92.7 ± 32.1	3.9 ± 0.3	4.2 ± 1.5	$\lesssim 7.1$
33.0	84.2 ± 32.6	3.4 ± 0.4	4.1 ± 1.6	$\lesssim 7.3$
40.6	70.6 ± 32.0	3.2 ± 0.5	4.5 ± 2.1	$\lesssim 8.7$
44.1	64.9 ± 31.4	3.3 ± 0.3	5.1 ± 2.5	$\lesssim 10.1$
60.8	43.4 ± 27.6	2.3 ± 0.7	5.4 ± 3.8	$\lesssim 12.9$

$\Pi_{\rm AME} \lesssim 1.2$ per cent for W49 at 44.1 GHz and $\Pi_{\rm AME} \lesssim 6.0$ per cent for W51 at 22.8 GHz. The constraint for W51 is quite loose and does not allow us to provide any strong claim on the nature of AME; the constraint for W49 is instead tighter, and favours the spinning dust model as the most plausible physical mechanism for AME. Follow up studies of W49 and W51 with higher resolution are required to better characterize their polarized emission, as the contamination from the observed polarized synchrotron is still the major factor hampering the measurement of a real AME polarized upper limit towards these region.

We conclude this section acknowledging that our polarization fractions may be underestimated, as the integration of the Stokes parameters inside the apertures may result in depolarization. To check for this effect, we can try and evaluate the level of possible aperture depolarization effects on the dust flux densities; we consider the *Planck* 353 GHz map, where the dust polarization flux densities are the highest. We then compute the (debiased) polarized intensity P for individual pixels in the region surrounding W49 and W51, and obtain a new estimate on the polarization of these sources by applying aperture photometry directly on the P map. For clarity, we shall label these new polarized flux densities as $P^{\rm (pix)}$, to stress that they are obtained integrating the values of individual pixels, while we refer to the flux densities we have employed up to now as $P^{\rm (ap)}$, as they are computed from the values of Q and U integrated over the apertures. Using the maps smoothed to a 1-deg resolution, and the same apertures as quoted in Table 1, we find $P^{\rm (pix)} = 181$ Jy for W49 and $P^{\rm (pix)} = 176$ Jy for W51, yielding, respectively, the polarization fractions $\Pi^{\rm (pix)} = 1.9$ per cent and $\Pi^{\rm (pix)} = 1.1$ per cent. These numbers are comparable with the estimates of $\Pi^{\rm (ap)}$ reported in Tables 5 and 6. Even when considering the *Planck* 353 GHz maps at their original

Downloaded from https://academic.oup.com/mnras/article/519/3/3432/6984761 by guest on 18 July 2023

resolution, we obtain $\Pi^{(ap)} = 1.0$ per cent and $\Pi^{(pix)} = 1.0$ per cent for W49, and $\Pi^{(ap)} = 1.2$ per cent and $\Pi^{(pix)} = 1.1$ per cent for W51 (in this case we are employing smaller apertures of $r_{ap} = 20$ arcmin for W49 and $r_{ap} = 30$ arcmin for W51, which are large enough to include the full extent of each source). Hence, integrating over our chosen apertures does not provide any evident depolarization effect for the dust emission. If we make the reasonable assumption that the polarization of AME, if present, would have the same orientation as the polarization of dust, we conclude that beam depolarization is not a major issue in our analysis.

Finally, we mention that also the mean orientation of the local magnetic field with respect to the plane of the sky affects the intrinsic level of dust polarization (Planck Collaboration VI 2020a), and is most likely the main reason for the low measured dust polarization fractions towards W49 and W51. This effect may also result in a low AME polarization in these particular sources. We then stress that the upper limits we quote in Table 12 could be a result of the geometrical configuration of the sources and the morphology of the local magnetic field, and cannot be used alone to infer a general property of AME polarization. A general, physical modelling of this foreground emission goes beyond the scope of this work. The results from Table 12 refer specifically to measurements obtained towards W49 and W51 at the angular scales set by our apertures (∼1 deg). The main conclusion of our study still remains that AME polarization is not detected towards W49 and W51 at this angular resolution, when considering the data set employed in this paper.

7 CONCLUSIONS

We have presented novel microwave intensity and polarization data for the Galactic regions W49, W51 and IC443 obtained with the QUIJOTE experiment; data were acquired with the MFI instrument at 11, 13, 17 and 19 GHz. This study is part of the QUIJOTE survey of astrophysically relevant Galactic regions, with the aim of characterizing the local foreground emission. In this case, the main goal was the assessment of the level of AME towards SNRs, and the estimate of the spectral index of synchrotron emission. The selected regions allow to compare different local environments: whereas IC443 is a relatively isolated SNR, W49 and W51 host SNRs in association with molecular clouds.

We described the observations performed with QUIJOTE and presented the resulting maps in the Stokes parameters I, Q and U towards the three regions. A null-test on the map allowed to confirm the good quality of these data products, as the computed sensitivity in polarization is consistent with the instrument specifications. The sources are well detected in total intensity; hints of polarized emission are visible towards W49, with a much more significant detection towards W51 and IC443. The inclusion of dedicated raster scan observations allow to reduce the noise level in polarization by a factor ∼2 in the source areas compared to the wide survey maps only.

We combined the QUIJOTE maps with a set of ancillary data to study the source properties in the frequency range [0.4, 3000] GHz. Flux densities for the Stokes parameters I, Q and U were measured on the maps with the aperture photometry technique, choosing aperture sizes suitable to each source angular extension and estimating the uncertainties as the rms of the flux densities from random apertures surrounding each source position. The polarization P and polarization fraction Π were obtained combining the Q and U values with a proper debiasing which ensures the final estimates are not overestimated. We also computed the polarization angle γ as a function of frequency.

The SEDs in total intensity were modelled with a multicomponent fit including different combinations of synchrotron, free–free, AME, CMB and thermal dust emission. We performed a similar fit on the polarized SEDs, where we considered possible contributions from synchrotron, AME and thermal dust. The highest frequency available for polarization data, 353 GHz, does not include the peak of the dust emission, implying the dust component would be poorly fitted; for this reason we fixed the dust temperature to the value obtained from the intensity SED prior to the fit.

For all three sources, the thermal dust component is well reconstructed in total intensity, with general agreement with the literature, while the synchrotron provides a good fit for the polarized SED, most likely proceeding from the local SNRs (or from diffuse Galactic emission in the case of W49). Still, we found that the total intensity SEDs for the sources W49 and W51 can be conveniently modelled without the inclusion of a synchrotron emission, confirming that the bulk of the local low-frequency emission is thermal; in W49, however, it is possible to accommodate a synchrotron component when fixing its spectral index to the value fitted on the polarized SED. We detected AME in these two regions, the QUIJOTE points proving crucial in confirming the downturn of AME emission at frequencies below 20 GHz. We employed *IRAS* and VLA data to assess the contribution of UCH II regions to the observed excess in the emission at microwave frequencies; this contamination is the main reason why W49 was discarded as a reliable AME source in Planck Collaboration XVI (2014a). We found that, although a measurable UCH II contribution is definitely present in our SEDs, its amplitude is not enough to account for the observed spectral bump at AME frequencies. We concluded that W49 and W51 host AME; this is the first time such claim is made for the W51 region (this result is also confirmed in Poidevin et al. 2022). However, we also acknowledged that, because our analysis has been conducted at a 1 deg resolution, it is not possible to assess whether AME proceeds indeed from the sources themselves, or enters our apertures from the neighbouring background. Still, our analysis confirms the presence of AME in total intensity towards these regions; tailored, higher resolution observations are required in order to better constrain its spatial origin.

We found that no AME contribution is required to improve the modelling of the polarized SEDs, thus confirming that polarized AME emission is not detected. We then derived conservative upper limits for the AME polarization fraction towards the two regions, finding $\Pi_{AME} \lesssim 1.2$ per cent for W49 at 44.1 GHz and $\Pi_{AME} \lesssim 6.0$ per cent for W51 at 22.8 GHz. The upper limit for W49 is relatively tight and suggests a very low or possibly null AME polarization; the upper limit for W51 is instead quite loose and non-informative in this sense. In reality, due to the confusion with the intervening polarized synchrotron emission, we expect both upper limits to be overestimated, thus favouring models of AME with a low degree of polarization (SDE or amorphous dust models). We also stressed that aperture depolarization may result in an actual underestimation of the AME polarization fractions, although a test performed for the polarized dust emission on *Planck* 353 GHz maps suggests this issue should not be too relevant. The main conclusion is that AME polarization is not detected in this study.

In the case of IC443, instead, we found that the intensity spectrum is best fitted by a combination of synchrotron, CMB and thermal dust, without any need for a free–free or AME contribution; the best modelling is achieved by introducing a break in the synchrotron spectrum. This result seems to confirm that AME is not naturally

Downloaded from https://academic.oup.com/mnras/article/519/3/3432/6984761 by guest on 18 July 2023

associated with SNRs, but more likely with dust-richer environments like molecular clouds; however, it is in tension with previous works that claimed an AME contribution is required to model the microwave spectrum of IC443. We discussed how such a claim could be the result of a systematic bias in the flux density measurements adopted in those works.

ACKNOWLEDGEMENTS

We thank the staff of the Teide Observatory for invaluable assistance in the commissioning and operation of QUIJOTE. The *QUIJOTE* experiment is being developed by the Instituto de Astrofisica de Canarias (IAC), the Instituto de Fisica de Cantabria (IFCA), and the Universities of Cantabria, Manchester and Cambridge. Partial financial support was provided by the Spanish Ministry of Science and Innovation under the projects AYA2007-68058-C03-01, AYA2007-68058-C03-02, AYA2010-21766-C03-01, AYA2010-21766-C03-02, AYA2014-60438-P, ESP2015-70646-C2-1-R, AYA2017-84185-P, ESP2017-83921-C2-1-R, AYA2017-90675-REDC (co-funded with EU FEDER funds), PGC2018-101814-B-I00, PID2019-110610RB-C21, PID2020-120514GB-I00, IACA13-3E-2336, IACA15-BE-3707, EQC2018-004918-P, the Severo Ochoa Programs SEV-2015-0548 and CEX2019-000920-S, the Maria de Maeztu Program MDM-2017-0765, and by the Consolider-Ingenio project CSD2010-00064 (EPI: Exploring the Physics of Inflation). We acknowledge support from the ACIISI, Consejeria de Economia, Conocimiento y Empleo del Gobierno de Canarias and the European Regional Development Fund (ERDF) under grant with reference ProID2020010108. This project has received funding from the European Union's Horizon 2020 research and innovation program under grant agreement number 687312 (RADIOFOREGROUNDS). DT acknowledges the support from the Chinese Academy of Sciences (CAS) President's International Fellowship Initiative (PIFI) with Grant N. 2020PM0042; DT also acknowledges the support from the South African Claude Leon Foundation, that partially funded this work. EdlH acknowledges partial financial support from the *Concepción Arenal Programme* of the Universidad de Cantabria. FG acknowledges funding from the European Research Council (ERC) under the European Union's Horizon 2020 research and innovation programme (grant agreement No 101001897). FP acknowledges the European Commission under the Marie Sklodowska-Curie Actions within the *European Union's Horizon 2020* research and innovation programme under Grant Agreement number 658499 (PolAME). FP acknowledges support from the Spanish State Research Agency (AEI) under grant numbers PID2019-105552RB-C43. BR-G acknowledges ASI-INFN Agreement 2014-037-R.0.

DATA AVAILABILITY STATEMENT

The QUIJOTE raster scan data at the core of this study are proprietary of the QUIJOTE Collaboration, however they are available on reasonable request to the corresponding author. The QUIJOTE nominal mode maps, which are also used in this analysis, are expected to be made publicly available in the first QUIJOTE data release. Other ancillary data employed in this work are publicly available and can be accessed online as detailed in the paper text.

REFERENCES

Abdo A. A. et al., 2009, ApJ, 706, L1
Ackermann M. et al., 2013, Science, 339, 807
Ade P. A. R. et al., 2021, Phys. Rev. Lett., 127, 151301
Aleksić J. et al., 2012, A&A, 541, A13
Ali-Haïmoud Y., 2013, Adv. Astron., 2013, 462697
Ali-Haïmoud Y., Hirata C. M., Dickinson C., 2009, MNRAS, 395, 1055
Ambrocio-Cruz P., Rosado M., de la Fuente E., Silva R., Blanco-Piñon A., 2017, MNRAS, 472, 51
AMI Consortium, 2009, MNRAS, 400, 1394
Battistelli E. S., Rebolo R., Rubiño-Martín J. A., Hildebrandt S. R., Watson R. A., Gutiérrez C., Hoyland R. J., 2006, ApJ, 645, L141
Battistelli E. S. et al., 2015, ApJ, 801, 111
Bennett C. L. et al., 2013, ApJS, 208, 20
Berkhuijsen E. M., 1972, A&AS, 5, 263
BICEP/Keck Collaboration, 2021, Phys. Rev. D, 103, 022004
Bik A., Henning T., Wu S. W., Zhang M., Brand ner W., Pasquali A., Stolte A., 2019, A&A, 624, A63
Binder B. A., Povich M. S., 2018, ApJ, 864, 136
Bonaldi A., Ricciardi S., Leach S., Stivoli F., Baccigalupi C., de Zotti G., 2007, MNRAS, 382, 1791
Bonatto C., Bica E., 2011, MNRAS, 414, 3769
Brogan C. L., Troland T. H., 2001, ApJ, 550, 799
Brogan C. L. et al., 2013, ApJ, 771, 91
Brun F., de Naurois M., Hofmann W., Carrigan S., Djannati-Ataï A., Ohm S., 2011, in Alecian G., Belkacem K., Samadi R., Valls-Gabaud D., eds, SF2A-2011: Proceedings of the Annual meeting of the French Society of Astronomy and Astrophysics. French Society of Astronomy and Astrophysics, Paris, p. 545
Carpenter J. M., Sanders D. B., 1998, AJ, 116, 1856
Casassus S., Cabrera G. F., Förster F., Pearson T. J., Readhead A. C. S., Dickinson C., 2006, ApJ, 639, 951
Casassus S. et al., 2008, MNRAS, 391, 1075
Castelletti G., Dubner G., Clarke T., Kassim N. E., 2011, A&A, 534, A21
Cepeda-Arroita R. et al., 2021, MNRAS, 503, 2927
Davies R. D., Dickinson C., Banday A. J., Jaffe T. R., Górski K. M., Davis R. J., 2006, MNRAS, 370, 1125
de Oliveira-Costa A., Tegmark M., Page L. A., Boughn S. P., 1998, ApJ, 509, L9
de Oliveira-Costa A., Tegmark M., Gutiérrez C. M., Jones A. W., Davies R. D., Lasenby A. N., Rebolo R., Watson R. A., 1999, ApJ, 527, L9
De Pree C. G. et al., 2018, ApJ, 863, L9
De Pree C. G. et al., 2020, AJ, 160, 234
Demetroullas C. et al., 2015, MNRAS, 453, 2082
Dickinson C. et al., 2009, ApJ, 690, 1585
Dickinson C., Peel M., Vidal M., 2011, MNRAS, 418, L35
Dickinson C. et al., 2018, New Astron. Rev., 80, 1
Draine B. T., 2011, Physics of the Interstellar and Intergalactic Medium. Princeton Univ. Press, Princeton
Draine B. T., Hensley B., 2013, ApJ, 765, 159
Draine B. T., Hensley B. S., 2016, ApJ, 831, 59
Draine B. T., Lazarian A., 1998, ApJ, 508, 157
Draine B. T., Lazarian A., 1999, ApJ, 512, 740
Dunham M. K. et al., 2010, ApJ, 717, 1157
Eden D. J. et al., 2018, MNRAS, 477, 3369
Egron E. et al., 2016, Supernova Remnants: An Odyssey in Space after Stellar Death, 18, Proceedings of the Conference held 6-11 June 2016, in Chania, Greece (arXiv:1609.03882)
Egron E. et al., 2017, MNRAS, 470, 1329
Fesen R. A., 1984, ApJ, 281, 658
Finkbeiner D. P., Schlegel D. J., Frank C., Heiles C., 2002, ApJ, 566, 898
Fixsen D. J., 2009, ApJ, 707, 916
Galván-Madrid R. et al., 2013, ApJ, 779, 121
Gao X. Y. et al., 2010, A&A, 515, A64
Gao X. Y., Han J. L., Reich W., Reich P., Sun X. H., Xiao L., 2011, A&A, 529, A159
Génova-Santos R., Rebolo R., Rubiño-Martín J. A., López-Caraballo C. H., Hildebrandt S. R., 2011, ApJ, 743, 67
Génova-Santos R., Rubiño-Martín J. A., Rebolo R., 2015a, Highlights of Spanish Astrophysics VIII, 207, Proceedings of the XI Scientific Meeting

Downloaded from https://academic.oup.com/mnras/article/519/3/3432/6984761 by guest on 18 July 2023

of the Spanish Astronomical Society held on September 8-12, 2014, in Teruel, Spain (arXiv:1504.03514)
Génova-Santos R., Rubiño-Martín J. A., Rebolo R., 2015b, MNRAS, 452, 4169
Génova-Santos R. et al., 2017, MNRAS, 464, 4107
Ginsburg A., 2017, Published in Star Formation Newsletter #290 (arXiv:1702.06627)
Ginsburg A., Bally J., Battersby C., Youngblood A., Darling J., Rosolowsky E., Arce H., Lebrón Santos M. E., 2015, A&A, 573, A106
Ginsburg A. et al., 2016, A&A, 595, A27
Ginsburg A. et al., 2017, ApJ, 842, 92
Ginsburg A. et al., 2020, ApJS, 248, 24
Goddi C., Ginsburg A., Maud L. T., Zhang Q., Zapata L. A., 2020, ApJ, 905, 25
González-Casanova D. F., De Colle F., Ramirez-Ruiz E., Lopez L. A., 2014, ApJ, 781, L26
Górski K. M., Hivon E., Banday A. J., Wandelt B. D., Hansen F. K., Reinecke M., Bartelmann M., 2005, ApJ, 622, 759
Greco E., Miceli M., Orlando S., Peres G., Troja E., Bocchino F., 2018, A&A, 615, A157
Green D. A., 1986, MNRAS, 221, 473
Green D. A., 2014, Bull. Astron. Soc. India, 42, 47
Guidi F. et al., 2021, MNRAS, 507, 3707
Gwinn C. R., Moran J. M., Reid M. J., 1992, ApJ, 393, 149
H. E. S. S. Collaboration, 2018, A&A, 612, A5
Hanabata Y., Sawada M., Katagiri H., Bamba A., Fukazawa Y., 2013, PASJ, 65, 42
Haslam C. G. T., Salter C. J., Stoffel H., Wilson W. E., 1982, A&AS, 47, 1
Hauser M. G. et al., 1998, ApJ, 508, 25
Hinshaw G. et al., 2013, ApJS, 208, 19
Hirayama A., Yamauchi S., Nobukawa K. K., Nobukawa M., Koyama K., 2019, PASJ, 71, 37
Hoang T., Lazarian A., 2016, ApJ, 821, 91
Hoang T., Draine B. T., Lazarian A., 2010, ApJ, 715, 1462
Hoang T., Lazarian A., Martin P. G., 2013, ApJ, 779, 152
Hoyland R. J. et al., 2012, in Holland W. S., ed., Proc. SPIE Conf. Ser. Vol. 8452, Millimeter, Submillimeter, and Far-Infrared Detectors and Instrumentation for Astronomy VI. SPIE, Bellingham, p. 845233
Huang Y., Li Z., Wang W., Zhao X., 2020, MNRAS, 492, 4246
Hwang U., Petre R., Hughes J. P., 2000, ApJ, 532, 970
Irfan M. O. et al., 2015, MNRAS, 448, 3572
Jacob A. M., Menten K. M., Wiesemeyer H., Ortiz-León G. N., 2021, A&A, 650, A133
Jonas J. L., Baart E. E., Nicolson G. D., 1998, MNRAS, 297, 977
Kamionkowski M., Kosowsky A., Stebbins A., 1997, Phys. Rev. D, 55, 7368
Keohane J. W., Reach W. T., Rho J., Jarrett T. H., 2007, ApJ, 654, 938
Kogut A. et al., 2007, ApJ, 665, 355
Kokusho T., Nagayama T., Kaneda H., Ishihara D., Lee H.-G., Onaka T., 2013, ApJ, 768, L8
Koo B.-C., Moon D.-S., 1997, ApJ, 475, 194
Koo B.-C., Kim K.-T., Seward F. D., 1995, ApJ, 447, 211
Koo B.-C., Lee J.-J., Seward F. D., Moon D.-S., 2005, ApJ, 633, 946
Koo B.-C., Kim C.-G., Park S., Ostriker E. C., 2020, ApJ, 905, 35
Krachmalnicoff N., Baccigalupi C., Aumont J., Bersanelli M., Mennella A., 2016, A&A, 588, A65
Kundu M. R., Velusamy T., 1967, Ann. Astrophys., 30, 59
Kundu M. R., Velusamy T., 1972, A&A, 20, 237
Kurtz S., Churchwell E., Wood D. O. S., 1994, ApJS, 91, 659
Lazarian A., Draine B. T., 2000, ApJ, 536, L15
Lee J.-J., Koo B.-C., Yun M. S., Stanimirović S., Heiles C., Heyer M., 2008, AJ, 135, 796
Lee Y.-H., Koo B.-C., Lee J.-J., 2020, AJ, 160, 263
Leitch E. M., Readhead A. C. S., Pearson T. J., Myers S. T., 1997, ApJ, 486, L23
Lim W., De Buizer J. M., 2019, ApJ, 873, 51
Lopez L. A., Ramirez-Ruiz E., Castro D., Pearson S., 2013, ApJ, 764, 50
López-Caraballo C. H., Rubiño-Martín J. A., Rebolo R., Génova-Santos R., 2011, ApJ, 729, 25
Loru S. et al., 2019, MNRAS, 482, 3857
Lozinskaya T. A., 1981, Sov. Astron. Lett., 7, 29
Macellari N., Pierpaoli E., Dickinson C., Vaillancourt J. E., 2011, MNRAS, 418, 888
Markwardt C. B., 2009, in Bohlender D. A., Durand D., Dowler P., eds, ASP Conf. Ser. Vol. 411, Astronomical Data Analysis Software and Systems XVIII. Astron. Soc. Pac., San Francisco, p. 251
Martin A. H. M., 1972, MNRAS, 157, 31
Mason B. S., Robishaw T., Heiles C., Finkbeiner D., Dickinson C., 2009, ApJ, 697, 1187
Matsumura H., Tanaka T., Uchida H., Okon H., Tsuru T. G., 2017, ApJ, 851, 73
Mehringer D. M., 1994, ApJS, 91, 713
Mezger P. G., Schraml J., Terzian Y., 1967, ApJ, 150, 807
Mitra D., Green D. A., Rao A. P., 2014, in Ray A., McCray R. A., eds, Proc. IAU Symp. 296, Supernova Environmental Impacts. Cambridge Univ. Press, Cambridge, p. 376
Moffett D. A., Reynolds S. P., 1994, ApJ, 437, 705
Mufson S. L., Liszt H. S., 1979, ApJ, 232, 451
Murphy E. J. et al., 2010, ApJ, 709, L108
Nashimoto M., Hattori M., Poidevin F., Génova-Santos R., 2020, ApJ, 900, L40
Okumura S.-i., Mori A., Nishihara E., Watanabe E., Yamashita T., 2000, ApJ, 543, 799
Olbert C. M., Clearfield C. R., Williams N. E., Keohane J. W., Frail D. A., 2001, ApJ, 554, L205
Onić D., Urošević D., Arbutina B., Leahy D., 2012, ApJ, 756, 61
Onić D., Urošević D., Leahy D., 2017, AJ, 153, 32
Penzias A. A., Jefferts K. B., Wilson R. W., 1971, ApJ, 165, 229
Petre R., Szymkowiak A. E., Seward F. D., Willingale R., 1988, ApJ, 335, 215
Planck Collaboration VIII, 2011, A&A, 536, A20
Planck Collaboration XVI, 2014a, A&A, 571, A13
Planck Collaboration XVI, 2014a, A&A, 565, A103
Planck Collaboration XIII, 2016b, A&A, 594, A1
Planck Collaboration XIII, 2016b, A&A, 594, A25
Planck Collaboration XIII, 2016c, A&A, 586, A134
Planck Collaboration VI, 2018, A&A, 610, C1
Planck Collaboration VI, 2020a, A&A, 641, A12
Planck Collaboration VI, 2020b, A&A, 641, A1
Planck Collaboration VI, 2020c, A&A, 641, A6
Planck Collaboration VI, 2020d, A&A, 643, A42
Planck Collaboration VI, 2020e, A&A, 641, A11
Platania P., Burigana C., Maino D., Caserini E., Bersanelli M., Cappellini B., Mennella A., 2003, A&A, 410, 847
Poidevin F. et al., 2019, MNRAS, 486, 462
Poidevin F., et al., 2022, MNRAS, 519, 3481
Purcell C. R. et al., 2013, ApJS, 205, 1
Pye J. P., Becker R. H., Seward F. D., Thomas N., 1984, MNRAS, 207, 649
Rajwade K., Seymour A., Lorimer D. R., Karastergiou A., Serylak M., McLaughlin M. A., Griessmeier J. M., 2016, MNRAS, 462, 2518
Ranasinghe S., Leahy D. A., 2018, AJ, 155, 204
Reich P., Reich W., 1986, A&AS, 63, 205
Reich P., Reich W., 1988, A&AS, 74, 7
Rho J., Petre R., 1998, ApJ, 503, L167
Ritchey A. M., Jenkins E. B., Federman S. R., Rice J. S., Caprioli D., Wallerstein G., 2020, ApJ, 897, 83
Rivera-Soto R., Galván-Madrid R., Ginsburg A., Kurtz S., 2020, ApJ, 899, 94
Rivilla V. M., Fontani F., Beltrán M. T., Vasyunin A., Caselli P., Martín-Pintado J., Cesaroni R., 2016, ApJ, 826, 161
Rivilla V. M., Beltrán M. T., Martín-Pintado J., Fontani F., Caselli P., Cesaroni R., 2017, A&A, 599, A26
Roberts H., van der Tak F. F. S., Fuller G. A., Plume R., Bayet E., 2011, A&A, 525, A107
Rubiño-Martín J. A., López-Caraballo C. H., Génova-Santos R., Rebolo R., 2012a, Adv. Astron., 2012, 351836

Downloaded from https://academic.oup.com/mnras/article/519/3/3432/6984761 by guest on 18 July 2023

Rubiño-Martín J. A. et al., 2012b, in Stepp L. M., Gilmozzi R., Hall H. J., eds, Proc. SPIE Conf. Ser. Vol. 8444, Ground-based and Airborne Telescopes IV. SPIE, Bellingham, p. 84442Y
Rubiño-Martín J. A. et al., 2017, in Arribas S., Alonso-Herrero A., Figueras F., Hernández-Monteagudo C., Sánchez-Lavega A., Pérez-Hoyos S., eds, Highlights on Spanish Astrophysics IX. Spanish Astronomical Society, Bilbao, Spain, p. 99
Rubiño-Martín J. A., et al., 2022, MNRAS, 517, 3916
Rugel M. R. et al., 2019, A&A, 622, A48
Rybicki G. B., Lightman A. P., 1979, Radiative Processes in Astrophysics. Wiley-VCH, Weinheim, Germany
Sano H. et al., 2021, ApJ, 919, 123
Saral G. et al., 2017, ApJ, 839, 108
Sato F., 1973, PASJ, 25, 135
Sato M., Reid M. J., Brunthaler A., Menten K. M., 2010, ApJ, 720, 1055
Seward F. D., 1990, ApJS, 73, 781
Siegel J., Dwarkadas V. V., Frank K. A., Burrows D. N., 2020, ApJ, 904, 175
Sievers A. W., Mezger P. G., Bordeon M. A., Kreysa E., Haslam C. G. T., Lemke R., 1991, A&A, 251, 231
Silsbee K., Ali-Haïmoud Y., Hirata C. M., 2011, MNRAS, 411, 2750
Simon R., Jackson J. M., Clemens D. P., Bania T. M., Heyer M. H., 2001, ApJ, 551, 747
Stevenson M. A., 2014, ApJ, 781, 113
Su Y., Fang M., Yang J., Zhou P., Chen Y., 2014, ApJ, 788, 122
Sun X. H., Reich W., Han J. L., Reich P., Wielebinski R., Wang C., Müller P., 2011, A&A, 527, A74
Tavani M. et al., 2010, ApJ, 710, L151
Tian W. W., Leahy D. A., 2013, ApJ, 769, L17
Tibbs C. T. et al., 2010, MNRAS, 402, 1969
Torres D. F., Romero G. E., Dame T. M., Combi J. A., Butt Y. M., 2003, Phys. Rep., 382, 303
Trujillo-Bueno J., Moreno-Insertis F., Sánchez F., eds, 2002, Astrophysical Spectropolarimetry. Cambridge Univ. Press, Cambridge
Ustamujic S., Orlando S., Greco E., Miceli M., Bocchino F., Tutone A., Peres G., 2021, A&A, 649, A14
Vaillancourt J. E., 2006, PASP, 118, 1340
Vastel C., Mookerjea B., Pety J., Gerin M., 2017, A&A, 597, A45
Vidal M. et al., 2011, MNRAS, 414, 2424
Vidal M., Dickinson C., Davies R. D., Leahy J. P., 2015, MNRAS, 452, 656
Vidal M., Dickinson C., Harper S. E., Casassus S., Witt A. N., 2020, MNRAS, 495, 1122
Watanabe Y., Nishimura Y., Harada N., Sakai N., Shimonishi T., Aikawa Y., Kawamura A., Yamamoto S., 2017, ApJ, 845, 116
Watson R. A., Rebolo R., Rubiño-Martín J. A., Hildebrandt S., Gutiérrez C. M., Fernández-Cerezo S., Hoyland R. J., Battistelli E. S., 2005, ApJ, 624, L89
Watts D. J. et al., 2015, ApJ, 814, 103
Westerhout G., 1958, Bull. Astron. Inst. Netherlands, 14, 215
Wilson T. L., Mezger P. G., Gardner F. F., Milne D. K., 1970, ApJ, 5, 99
Wilson T. L., Rohlfs K., Hüttemeister S., 2009, Tools of Radio Astronomy. Springer, Berlin
Wolleben M., Landecker T. L., Reich W., Wielebinski R., 2006, A&A, 448, 411
Wu S.-W., Bik A., Bestenlehner J. M., Henning T., Pasquali A., Brandner W., Stolte A., 2016, A&A, 589, A16
Xu Y., Reid M. J., Menten K. M., Brunthaler A., Zheng X. W., Moscadelli L., 2009, ApJ, 693, 413
Yoshiike S., Fukuda T., Sano H., Fukui Y., 2017, 6th International Symposium on High Energy Gamma-Ray Astronomy, AIP Conference Proceedings, vol. 1792, p. 040039
Ysard N., Verstraete L., 2010, A&A, 509, A12
Zaldarriaga M., Seljak U., 1997, Phys. Rev. D, 55, 1830
Zhang B., Reid M. J., Menten K. M., Zheng X. W., Brunthaler A., Dame T. M., Xu Y., 2013, ApJ, 775, 79
Zhang M. F., Tian W. W., Leahy D. A., Zhu H., Cui X. H., Shan S. S., 2017, ApJ, 849, 147
Zhang S. et al., 2018, ApJ, 859, 141
Zhou X., Miceli M., Bocchino F., Orland o S., Chen Y., 2011, MNRAS, 415, 244
Zhu H., Tian W. W., Zuo P., 2014, ApJ, 793, 95

APPENDIX A: FLUX CONTRIBUTION FROM NEIGHBOURING AREAS

As already mentioned in the beginning of Section 6.3, given the common resolution of 1 deg that we adopt throughout the frequency range we explore, the AME signal we detect towards W49 and W51 may have a significant contribution coming from the Galactic emission that surrounds them. In this section, we shall refer to the area surrounding each source, with the exclusion of the source itself, as the 'region'. Although it is not possible to extract further information about the actual spatial distribution of the measured flux densities, we can still get a rough estimate of the level of the region contribution in our chosen apertures.

We repeat the measurement of the flux densities of W49 and W51, using this time the maps prior to the convolution with a 1-deg beam. We focus in particular on the maps with the highest original resolution, where the sources are better resolved; we set the threshold $\theta_{\rm FWHM} < 10$ arcmin, which selects the Urumqi map at low frequencies and the *Planck*-HFI maps at higher frequencies. This time we can choose a smaller aperture, in order to only encompass the source angular extent; we select an internal radius of $r_{\rm ap} = 20$ arcmin for W49 and $r_{\rm ap} = 30$ arcmin for W51. These values are chosen to ensure each source is completely encompassed by the aperture, and they are slightly larger than the nominal source diameters because

Table A1. Evaluation of the region contribution in our apertures at different frequencies, towards W49 and W51. For each case we report the considered survey and frequency, the original map resolution, the flux density $S_{\rm or}$ from the original maps, the flux density $S_{\rm 1d}$ measured on the 1-deg smoothed maps, and the fractional contribution of the region flux density $\Delta S/S_{\rm 1d}$ to the reference measurement on the smoothed maps. For the measurement of the original resolution fluxes, we adopt an aperture radius $r_{\rm ap} = 20$ arcmin for W49 and $r_{\rm ap} = 30$ arcmin for W51.

			W49			W51		
Survey	Freq. (GHz)	Reso. (arcmin)	$S_{\rm or}$ (Jy)	$S_{\rm 1d}$ (Jy)	$\Delta S/S_{\rm 1d}$ (per cent)	$S_{\rm or}$ (Jy)	$S_{\rm 1d}$ (Jy)	$\Delta S/S_{\rm 1d}$ (per cent)
Urumqi	4.8	9.5	90.1	150.5	40.1	473.6	657.9	28.0
Planck	100	9.7	90.4	220.5	59.0	322.3	530.0	39.2
Planck	143	7.3	150.9	493.8	69.4	431.8	957.7	54.9
Planck	217	5.0	510.1	2021.9	74.8	1244.6	3545.3	64.9
Planck	353	4.9	2326.0	9666.2	75.9	5300.1	$(1.6) \times 10^4$	67.4
Planck	545	4.8	8734.7	$(3.6) \times 10^4$	75.6	$(2.1) \times 10^4$	$(6.1) \times 10^4$	65.5
Planck	857	4.6	$(3.0) \times 10^4$	$(1.2) \times 10^5$	74.6	$(7.5) \times 10^4$	$(2.1) \times 10^5$	63.4

Downloaded from https://academic.oup.com/mnras/article/519/3/3432/6984761 by guest on 18 July 2023

even these smaller beams produce a broadening of the source signal to some extent. The background annulus is chosen in each case with a separation of 20 arcmin from the aperture, and with a size of 20 arcmin (i.e. $r_{\rm int} = r_{\rm ap} + 20$ arcmin and $r_{\rm ext} = r_{\rm int} + 20$ arcmin). The comparison of the flux densities computed this way and the ones computed on the 1-deg smoothed maps with the nominal apertures, shown in Table 1, enables us to obtain information on the typical region contribution in our measurements.

The results are summarized in Table A1, where for each of the selected maps we report its original FWHM value, the flux densities $S_{\rm or}$ computed on the map at its parent angular resolution, and the flux densities $S_{\rm 1d}$ computed on the 1-deg smoothed map. The difference $S_{\rm 1d} - S_{\rm or}$ is our estimate of the flux proceeding from the region that makes it into our apertures; it is reported in Table A1 as a fractional contribution with respect to the 1-deg flux $S_{\rm 1d}$. In Fig. A1 we also show, for three sample frequencies, the comparison between the maps at their original resolution and the smoothed maps, together with the circles employed for the photometric analysis in each case.

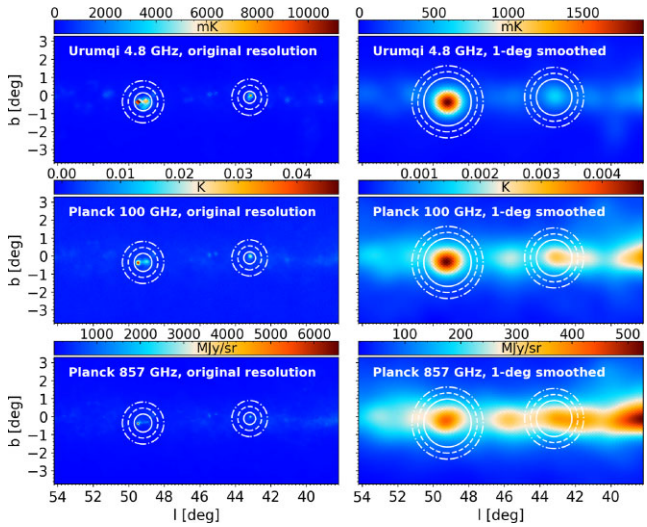

Figure A1. A comparison between the maps at their original resolution (left-hand panel) and smoothed to a 1-deg beam (right-hand panel) for three sample frequencies, in the area encompassing W49 and W51. The apertures employed to compute the flux densities reported in Table A1 are also shown.

We notice that the fractional region flux density in our apertures is in general larger than 50 per cent. Now, because this is the total flux, which results from the combination of different emission mechanisms, we cannot say that this is the fraction of background AME that enters the apertures. In fact, the ratios tend to be larger at higher frequencies, where we are practically dominated by thermal dust emission and we expect indeed a significant contribution from the diffuse Galactic dust (Planck Collaboration XIII 2016b). On the contrary, at the Urumqi frequency, in these regions we are dominated by free–free emission, which is also a relevant component of the diffuse emission.

These results show that it is indeed likely that a contribution of the AME signal does not come from our sources; still, it is not possible to rule out the presence of AME in the molecular clouds associated with W49 and W51. As already mentioned, we are limited by the coarser resolution of most of the surveys we consider, and it is not possible to circumvent this issue. We stress in particular that similar analyses we have cited in the text are affected by the same type of uncertainty (e.g. Planck Collaboration XVI 2014a; Demetroullas et al. 2015; Planck Collaboration XIII 2016c). In our case, we ensured we acknowledge this issue when presenting our results.

This paper has been typeset from a TEX/LATEX file prepared by the author.

Downloaded from https://academic.oup.com/mnras/article/519/3/3432/6984761 by guest on 18 July 2023